Structure and functional determinants of Rad6–Bre1 subunits in the histone H2B ubiquitin-conjugating complex

Prakash K. Shukla[1,2], **Jesse E. Bissell**[1,2], **Sanjit Kumar**[3], **Srijana Pokhrel**[1,2], **Sowmiya Palani**[1,2], **Kaitlin S. Radmall**[1,2], **Onyeka Obidi**[4], **Timothy J. Parnell**[2], **Julia Brasch**[4], **Dennis C. Shrieve**[1] and **Mahesh B. Chandrasekharan** [ID][1,2,*]

[1]Department of Radiation Oncology, University of Utah School of Medicine, Salt Lake City, UT 84112, USA, [2]Huntsman Cancer Institute, University of Utah School of Medicine, Salt Lake City, UT 84112, USA, [3]Centre for Bioseparation Technology, Vellore Institute of Technology, Vellore, Tamil Nadu 632014, India and [4]Department of Biochemistry, University of Utah School of Medicine, Salt Lake City, UT 84112, USA

ABSTRACT

The conserved complex of the Rad6 E2 ubiquitin-conjugating enzyme and the Bre1 E3 ubiquitin ligase catalyzes histone H2B monoubiquitination (H2Bub1), which regulates chromatin dynamics during transcription and other nuclear processes. Here, we report a crystal structure of Rad6 and the non-RING domain N-terminal region of Bre1, which shows an asymmetric homodimer of Bre1 contacting a conserved loop on the Rad6 'backside'. This contact is distant from the Rad6 catalytic site and is the location of mutations that impair telomeric silencing in yeast. Mutational analyses validated the importance of this contact for the Rad6–Bre1 interaction, chromatin-binding dynamics, H2Bub1 formation and gene expression. Moreover, the non-RING N-terminal region of Bre1 is sufficient to confer nucleosome binding ability to Rad6 *in vitro*. Interestingly, Rad6 P43L protein, an interaction interface mutant and equivalent to a cancer mutation in the human homolog, bound Bre1 5-fold more tightly than native Rad6 *in vitro*, but showed reduced chromatin association of Bre1 and reduced levels of H2Bub1 *in vivo*. These surprising observations imply conformational transitions of the Rad6–Bre1 complex during its chromatin-associated functional cycle, and reveal the differential effects of specific disease-relevant mutations on the chromatin-bound and unbound states. Overall, our study provides structural insights into Rad6–Bre1 interaction through a novel interface that is important for their biochemical and biological responses.

GRAPHICAL ABSTRACT
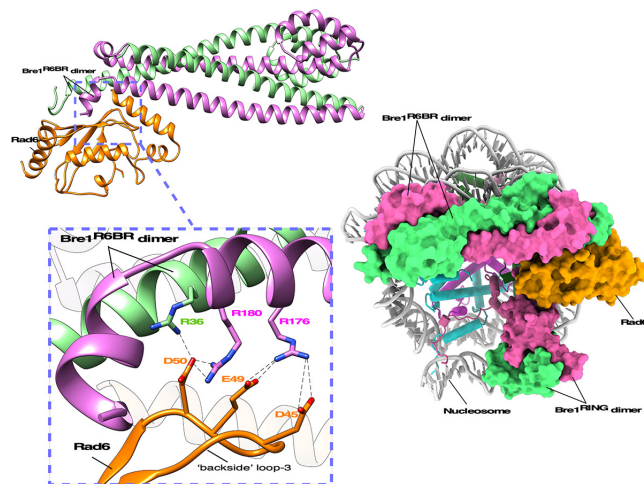
INTRODUCTION

Post-translational modifications of histone proteins regulate chromatin structure and transactions during development and disease pathogenesis including cancers (1,2). Monoubiquitination of histone H2B lysine123 (K123) in the yeast *Saccharomyces cerevisiae* or K120 in mammals is crucial for proper gene transcription (3), and is also linked to DNA replication, repair and recombination (4,5). Histone H2B monoubiquitination (H2Bub1) controls nucleosome stability (6) and chromatin dynamics (7,8), and the *trans*-histone regulation of H3K4 and H3K79 methylation (9–12). In yeast, the histone H2B ubiquitin-conjugating (HUC) complex comprises the Rad6 E2 ubiquitin-conjugating enzyme, a homodimer of the Bre1 RING-type E3 ubiquitin ligase and the accessory protein

*To whom correspondence should be addressed. Tel: +1 801 213 4220; Fax: +1 801 585 0900; Email: mahesh.chandrasekharan@hci.utah.edu

Lge1 ([13,14]). The orthologous complex in humans comprises UBE2A/UBE2B, RNF20-RNF40 and WAC ([15]), respectively, each of which is mutated or misregulated in cancers and other diseases.

In order to advance our fundamental understanding of the HUC complex, we have determined the X-ray crystal structure of Rad6 in complex with a non-RING domain N-terminal region (amino acids 1–212) of Bre1, which is necessary and sufficient to bind Rad6 *in vitro* ([16]) and potentiate ubiquitin transfer to substrate H2B ([17]). Interestingly, our structure reveals a heteromeric configuration of the Bre1 homodimer, which thus mimics the heterodimers of its homologs present in fission yeast and human HUC complexes ([15,18]). Our structure further uncovers that the N-terminal non-RING domain Rad6-binding regions (R6BRs) of the Bre1 E3 ligase use a two-helix-based mode of interaction to bind a single unit of partner Rad6 E2 enzyme, which is distinct from other known E2 'backside' binders. We used structural insights to guide our biochemical, genetics and genomics studies, and uncovered the molecular basis, biological importance and the chromatin-based interaction dynamics for the Rad6–Bre1 complex. We demonstrate that association with Bre1^{R6BR} is sufficient to confer nucleosome binding ability to Rad6, which reveals a substrate recognition function for a non-RING domain region within an E3 ubiquitin ligase. Our studies also show that certain cancer-relevant interaction-interface mutations in Rad6 increase Rad6–Bre1 association in solution but disrupt it on chromatin, thus revealing new facets for Rad6–Bre1 interaction dynamics and a novel mode of pleiotropy for disease-relevant mutations that can differentially influence a protein's functions in its chromatin-bound and unbound states.

MATERIALS AND METHODS

Plasmid construction

A DNA fragment containing sequences for the Flag epitope-tag, a stop codon and the *RAD6* terminator region (450 bp) along with SpeI–BamHI sites at the 5′ end and KpnI site at the 3′ end was obtained by polymerase chain reaction (PCR) using yeast genomic DNA as the template. The PCR product was then digested with SpeI–KpnI and inserted into the same sites in pRS314 (*TRP1*, CEN). Into this construct, the *RAD6* promoter region (286 bp) was inserted as a NotI–SpeI-digested fragment following its PCR amplification from yeast genomic DNA to obtain the construct pMC5 (*RAD6prom-Spe1-BamH1-Flag-RAD6term*, *TRP1* CEN). The sequence for the Flag-epitope from the parent plasmid was replaced with a sequence coding for three copies of the V5 epitope-tag using an Integrated DNA Technologies (IDT) gblocks® gene fragment, to obtain construct pMC6.

A gblocks® fragment for the *RAD6* coding region was synthesized to contain SpeI and BamHI sites at the 5′ and 3′ ends, respectively, a 20 bp sequence homologous to that adjacent to SpeI and BamHI sites in pMC5 and, additionally, contain translationally silent BclI and XhoI sites near the sequence coding for Rad6's backside loop (amino acids 42–51). This modified *RAD6* open reading frame (ORF) gblocks® fragment was inserted into SpeI–BamHI-digested pMC5 by sequence and ligation independent cloning (SLIC) ([19]) to obtain construct pMC7, which was propagated in *Escherichia coli dam− dcm–* (NEB). Point mutations were introduced into *RAD6* using annealed oligonucleotides ligated to BclI–XhoI-digested pMC7. Alternatively, mutants were generated using gblocks® gene fragments with the introduced mutations to replace the *RAD6* coding sequence in pMC7. To change the epitope-tag, the *RAD6* coding region (wild type or mutant) was inserted as a SpeI–BamHI-digested fragment into pMC6.

To create Bre1 expression constructs, the 700 bp *BRE1* promoter region upstream of the ATG codon was PCR amplified to contain SacI and SpeI at its 5′ and 3′ end, respectively. The PCR product was digested with SacI and SpeI, and inserted into the same sites in p415ADH, LEU and CEN ([20]) to replace the *ADH1* promoter, resulting in construct *BRE1prom-Spe1-HindIII-CYC1term* (pMC8). The *BRE1* coding region was then PCR amplified using yeast genomic DNA as the template and inserted into pMC8 following SpeI–HindIII digestion to obtain construct pMC9. This construct was used to create Bre1 point or truncation mutants using SLIC, where the IDT gblocks® fragment harboring a portion of *BRE1* with the introduced mutation replaced the wild-type sequence between SpeI–NdeI sites.

For co-expression of Rad6 and Bre1, the *RAD6* coding region (amino acids 1–150) was PCR amplified and inserted by SLIC into BamHI–NotI sites in pRSF-Duet (Novagen). Subsequently, either full-length *BRE1* or a fragment of *BRE1* (coding for amino acids 1–212; Bre1$^{1–212}$ or Bre1^{R6BR}) was PCR amplified and inserted downstream between BglII–XhoI sites using SLIC to obtain construct pMC10. For expression and purification of biotinylated Bre1, a gblocks® fragment was synthesized to contain a sequence coding for Bre1 (amino acids 152–212) and the 15 amino acid biotinylation sequence [AviTag™ ([21])] and then inserted into MfeI–XhoI-digested pMC10. To express and purify Bre1 for custom antibody generation, the *BRE1* coding region minus the RING domain (amino acids 1–645) was inserted into pETM-14 (EMBL) using SLIC. Constructs for UBE2A or UBE2A-P43L with three copies of the V5 epitope-tag at their N-terminus in pTwist-EF1alpha were created using Twist Bioscience.

An IDT gblocks® fragment was synthesized to encode Protein A/G (PAG) fusion protein containing five IgG-binding domains from *Staphylococcus aureus* Protein A and two IgG-binding domains from *Streptococcus* Protein G, and codon-optimized for expression in yeast. The coding region for *Candida RAD6* (*CAGL0I00352g*) was PCR amplified from *Candida glabrata* genomic DNA along with flanking 20 bp sequences homologous to the vector backbone or the PAG gblocks® fragment. This PCR product and the PAG gblocks® fragment were then inserted by SLIC into the SpeI–BamHI-digested *C. glabrata* expression plasmid pCN-PDC1 ([22]) (a gift from Brendan Cormack; Addgene # 45325), to obtain construct pMC11.

All plasmid constructs were confirmed by Sanger sequencing.

Yeast strains and media

Genotypes of yeast strains are listed in Supplementary Table S2. Yeast cells were grown in YPAD broth (1% yeast

extract, 2% peptone, 2% dextrose and 0.004% adenine hemisulfate) or in synthetic dropout (SD) media. Solid media were prepared by adding 2% agar to liquid broth. *Saccharomyces cerevisiae* and *C. glabrata* were grown at 30°C. To create gene knockout strains, the coding region of a target gene was deleted in parental YMH171 and/or DHY214/DHY217 or their derivative strains using PCR products containing the disrupted locus and the replacement *KanMX6* selection cassette amplified from genomic DNA isolated from the respective deletion mutant in Open Biosystem's yeast collection. Alternatively, a one-step PCR-based gene knockout strategy was performed using pF6a-KanMX or pAG25 (23) as template. Also, the *RAD6* coding region was replaced with a *URA3* gene using a construct containing the *RAD6* promoter and terminator sequences flanking *URA3* and linearized with HindIII–BamHI prior to transformation. To create strain YMC1, the *HIS3MX6* selection module along with ∼40 bp sequences homologous to the *BRE1* promoter and 3′-terminator regions was amplified using pYM15 as the template and transformed into YZS363. To create strain YZS406, the *klTRP1* selection module along with ∼40 bp sequences homologous to the *BRE1* promoter and 3′-terminator regions was amplified using pYM3 as the template and transformed into YZS375. All plasmids and yeast strains described in this study are available upon request.

Spotting assays

Telomeric silencing reporter strain YZS377 was transformed with either vector pRS314 (*TRP1*, CEN) (24) alone or pMC5 derivatives containing either wild-type *RAD6* or its various mutants. Likewise, telomeric silencing reporter strain YMC1 was transformed with either vector pMC8 (*LEU*, CEN) alone or pMC9 derivatives containing either wild-type *BRE1* or its mutants. These strains were grown overnight at 30°C with constant shaking in liquid SD media lacking tryptophan or leucine (-TRP or -LEU). Cells (1 OD_{600} or 1×10^7) were harvested, and a 10-fold serial dilution was performed prior to spotting them onto solid -TRP or -LEU media. For silencing assay, the media additionally contained 5-fluoroorotic acid (5-FOA), and cells were grown at 30°C for 2–3 days.

Protein expression

The pET28a- or pRSF-Duet-based constructs were transformed into *E. coli* BL21-CodonPlus (DE3)-RIL (Agilent Technologies) to express His_6Rad6 or its mutant derivatives, or His_6Rad6 with either $Bre1^{R6BR}$ or biotinylated $Bre1^{R6BR}$. Bacteria were cultured in Luria Broth (LB) containing kanamycin (50 μg/ml) and chloramphenicol (10 μg/ml) with shaking at 37°C and induced with 0.25 mM isopropyl-β-D-thiogalactopyranoside (IPTG; GoldBio) at an $OD_{600\,nm}$ of 0.6, followed by overnight growth at 16°C. For expression of biotinylated $Bre1^{R6BR}$, the medium was supplemented with 0.05 mM D-biotin (Fisher Scientific) upon induction with IPTG.

Selenomethionine (SeMet)-substituted His_6Rad6–$Bre1^{R6BR}$ was expressed in *E. coli* B843 (DE3). Following culture in minimal medium containing methionine to $OD_{600\,nm}$ 0.6, cells were harvested by centrifugation, resuspended in fresh minimal medium lacking methionine and cultured for 2 h before addition of SeMet to 50 mg/ml and for an additional 4 h before induction with 0.25 mM IPTG. Following purification, >99% SeMet incorporation into both His_6Rad6 and $Bre1^{R6BR}$ was confirmed by electrospray ionization/mass spectrometry (ESI/MS).

Protein purification

All protein variants were purified using the same method. Whole-cell lysate from bacterial cell pellets was resuspended in a lysis buffer [25 mM Tris–HCl pH 7.9, 150 mM NaCl, 20 mM imidazole, 1 mM phenylmethylsulfonyl fluoride (PMSF)], digested with lysozyme (Sigma) for 20 min on ice and sonicated using a Misonix Sonifier. For purification of His_6Bre1^{1-645}, the lysis buffer additionally contained 1% Triton X-100. The soluble fraction was then obtained by high-speed centrifugation (40 000 rpm, 30 min at 4°C) using a Ti45 rotor in a Beckman Optima™L90-K Ultracentrifuge. The supernatant was loaded onto a nickel affinity column (HisTrap™ FF, GE Healthcare), washed with 20 column volumes of lysis buffer and eluted with a 20–500 mM imidazole gradient. Fractions from all chromatographic steps were evaluated by sodium dodecylsulfate–polyacrylamide gel electrophoresis (SDS–PAGE). Thrombin (10 U; Sigma) was added to the protein solution as needed to remove the affinity tag, which was dialyzed overnight at 4°C into a buffer containing 25 mM Tris–HCl pH 7.9, 50 mM KCl, 10% glycerol, 1 mM EDTA and 1 mM dithiothreitol (DTT). Dialysate was centrifuged (40 000 rpm, 30 min at 4°C), loaded onto a Mono Q anion exchange column (GE Healthcare) and eluted with a 50–1000 mM KCl gradient. The final chromatography step was purification by size exclusion chromatography (SEC) on a Superdex™ 75 column (GE Healthcare) in a buffer containing 25 mM Tris–HCl pH 7.9, 100 mM NaCl, 10% glycerol, 1 mM EDTA and 1 mM [tris(2-carboxyethyl)phosphine] (TCEP) (SEC buffer). The purified protein was concentrated using a Vivaspin 10 kDa MWCO Centrifugal Concentrator.

For biolayer interferometry, the biotinylated $Bre1^{R6BR}$ was obtained by co-expression and co-purification of the His_6Rad6–$Bre1^{R6BR}$biotin, followed by resuspension in a denaturant buffer (25 mM Tris–HCl pH 7.9, 100 mM NaCl, 10% glycerol, 2 M urea, 1 mM EDTA and 1 mM TCEP) and incubation on ice for 1 h. Fractions containing $Bre1^{R6BR}$biotin were dialyzed overnight against SEC buffer, and further purified on a Superdex 200™ column in SEC buffer lacking glycerol. The fractions with $Bre1^{R6BR}$biotin were combined and concentrated using a Vivaspin 30 kDa MWCO Centrifugal Concentrator.

Crystallization and data collection

Our crystallization trials with unmodified protein failed. We therefore incubated His_6Rad6–$Bre1^{R6BR}$ (4 mg/ml) with Proteinase K (25) at a 1000:1 molar ratio at room temperature for 30 min, and repurified it on a Superdex 200 column. SDS–PAGE revealed bands indicating His_6Rad6, $Bre1^{R6BR}$ and an equal part of a truncated Bre1. ESI/MS analysis

indicated that some Bre1 had been cleaved after residue 186, producing Bre1$^{1–186}$ (Supplementary Figure S3a–c).

Partially proteolyzed Rad6–Bre1 was concentrated to 4 mg/ml in SEC buffer. Crystallization conditions were screened by sitting-drop vapor diffusion using a Gryphon crystallization robot (Art Robbins Instruments). After optimization of crystals first seen in the JCSG + screen, condition H11, reproducible crystals appeared overnight at 13°C after mixing 1 μl of protein with 1 μl of crystallization buffer #1 [0.1 M MgCl$_2$, 0.1 M Tris-bis pH 5.5, 25% (v/v) polyethylene glycol (PEG) 3350] in a 24-well sitting-drop vapor diffusion crystallization plate (Hampton Scientific HR3-114) against a 1 ml reservoir of crystallization buffer #1.

Crystals were immersed (20 s) in reservoir solution supplemented with 25% glycerol prior to plunging into liquid nitrogen. Data collection was performed at the Stanford Synchrotron Radiation Lightsource (SSRL). Data were integrated and scaled using XDS and AIMLESS (26). Crystals belonged to space group P3$_1$12 ($a = b = 127$ Å, $c = 198$ Å) with three copies of the complex in the asymmetric unit. The data exhibited translational pseudo-symmetry where the pseudo-cell could be indexed in space group P3$_1$21 ($a = b = 73$ Å, $c = 198$ Å) with one copy of the complex in the asymmetric unit, although structure determination (below) was performed in the true space group.

To improve crystal quality, Rad6–Bre1 was reductively methylated as follows: His$_6$Rad6–Bre1 in SEC buffer was dialyzed against 50 mM HEPES pH 7.6, 100 mM NaCl, 10% glycerol, 1 mM EDTA and 1 mM TCEP according to the Hampton Research protocol. Dimethylamine-borane (DMAB) complex (20 μl, 1 M) and methanol-free formaldehyde (40 μl, 1 M) were added, and the protein sample was placed on ice in an aluminum foil-wrapped tube for 2 h, after which an additional 40 μl of DMAB complex was added and the reaction was incubated in the dark and on ice overnight. The reaction was quenched by addition of 500 μl of 1 M glycine, and the protein repurified by SEC. ESI/MS indicated ∼27 methylation sites in Bre1^{R6BR} and ∼10 sites in His$_6$Rad6. This methylated (m) protein was concentrated, proteolyzed and re-purified by SEC as described for the unmodified protein. mHis$_6$Rad6–Bre1$^{1–212}$–Bre1$^{1–186}$ crystallized against a reservoir of 0.05–0.1 M MMT buffer and 15–25% PEG400 (crystallization buffer #2). Crystal mounting and data collection were performed as for the unmethylated protein. Diffraction data was extended to 2.7 Å resolution and were indexed in space group P2$_1$2$_1$2 ($a = 241$ Å, $b = 49$ Å, $c = 57$ Å) with one copy of the complex in the asymmetric unit.

To confirm the protein sequence and the chain directionality in the built model, leucine-to-methionine point mutations were introduced into Bre1^{R6BR} for SeMet incorporation. Several constructs were tested, but only Bre1^{R6BR} double mutants L146M + L153M or L160M + L167M formed a stable complex with Rad6. These complexes were expressed in bacteria to contain SeMet, purified, proteolyzed and re-purified in the same manner as described above. The mutated Rad6–Bre1-containing proteins crystallized in the trigonal crystal form. For heavy-atom modifications, crystals were briefly soaked (5–10 min) in mother liquor supplemented with cryoprotectant and 0.1–0.5 mM Thimerosal or

K$_2$PtCl$_4$. All data were collected at SSRL. X-ray energies were chosen to optimize anomalous scattering from Se, Hg or Pt as appropriate to the crystal.

Structure determination

An initial structure of a single unmethylated SeMetHis$_6$Rad6–Bre1$^{1–212}$–Bre1$^{1–186}$ protein was determined using single-wavelength anomalous diffraction (SAD) in the true trigonal crystal form (three molecules per asymmetric unit). For this crystal, data were collected on SSRL beamline 9–2 at a wavelength of 0.9792 Å. The data were analyzed with the program CRANK (27) (part of the CCP4i analysis package). Initial phases were calculated using 29 selenium sites and were improved by density modification. The experimental F_{obs} electron density map, calculated at 3.1 Å resolution, showed clear helical density and other features that enable model building. As part of the CRANK routine, automatic model building was performed by Buccaneer (28), autosol (29) and autobuild (30). A model of Rad6 (PDB: 1AYZ) was easily superimposed in three positions on the resulting autobuild model. Selenium sites corresponded to Rad6 methionine residues (six per molecule). Examination of the auto-build model and the experimental electron density showed a bundle of four helices corresponding to Bre1 associated with each Rad6 monomer. Several selenium sites fell within the region of Bre1, indicating the positions of methionine residues within this protein. This initial model was modified by iterative rounds of manual model building with Coot (31) and refinement with phenix.refine (32) that resulted in a structure containing three Rad6 molecules and 12 long helices of Bre1 dimers. The orientation of helices and assignment of the Bre1 sequence were not clear at this stage, and R_{work}/R_{free} remained at 0.42/0.50.

The final reported structure of the methylated protein in the orthorhombic crystal form was determined by molecular replacement using a model of Rad6 (PDB: 1AYZ) and the program Phaser (33) (Z-score = 7.0). A copy of the partial complex from the trigonal crystal structure was superimposed on the resulting molecular replacement solution. This model did not display steric clashes with symmetry-related molecules, and the Rad6-phased map followed clear helical density for the partial model of Bre1. Subsequent rounds of model building and refinement resulted in a near complete model. To assist in model building, anomalous difference maps from SeMet and platinum- or mercury-soaked crystals as described above were used to verify cysteine and methionine positions. This permitted assignment of the directions of the helices and confirmed the positions of key residues of Bre1. This model of mHis$_6$Rad6–Bre1$^{1–212}$–Bre1$^{1–186}$ was refined to R_{work} = 0.239 and R_{free} = 0.279 (Supplementary Table S1). The Ramachandran statistics were refined, and the model was analyzed using PROCHECK (34). A total of 97% of residues were in the most favored regions and 3% in the additional allowed regions for mHis$_6$Rad6–Bre1$^{1–212}$–Bre1$^{1–186}$ (PDB: 7UV8). A total of 96% of residues were in the most favored regions and 4% in the additional allowed regions for mHis$_6$Rad6P43L–Bre1$^{1–212}$–Bre1$^{1–186}$ (PDB: 7UVC).

Structures were aligned using the SUPERPOSE (35) program of CCP4i. Buried surface areas were calculated using NACCESS (36) and COCOMAPS (37). Figures were generated using UCSF Chimera or Pymol. Atomic distances were determined using LigPlot+ (38).

Immunoblotting

To examine the steady-state levels of proteins or histone modifications, yeast cell extracts were prepared in SUME buffer [10 mM MOPS pH 6.8, 0.5% SDS, 8 M urea, 10 mM EDTA, protease inhibitors (1 mM PMSF, 1 μg/ml aprotinin, 1 μg/ml leupeptin, 1 μg/ml pepstatin A)] using the bead-beating procedure as described (39). Histone H2B ubiquitination levels in yeast cells were examined as described (40). Briefly, yeast cells (40×10^7) were harvested, washed once with phosphate-buffered saline (PBS) and once with 5% tricholoroacetic acid (TCA, Sigma) before storage at $–80°C$. Cell pellets were thawed in 20% TCA, lysed by bead beating, and centrifuged (3000 rpm, 5 min at $4°C$). The pellet was resuspended in $1\times$ Laemmli buffer (62.5 mM Tris–HCl pH 6.8, 10% glycerol, 2% SDS, 0.002% bromophenol blue, 5% β-mercaptoethanol). The resulting solution was neutralized by adding 2 M Tris base before boiling for 8 min in a water bath and clarified by centrifugation (13 200 rpm, 10 min at $4°C$). Protein concentration of the lysate was measured using DC™ Protein Assay (Bio-Rad). Equal amounts of proteins from various samples were resolved in SDS–PAGE and transferred onto a polyvinylidene difluoride (PVDF) membrane. Following incubation with primary antibody and corresponding horseradish peroxidase (HRP)-conjugated secondary antibody, protein signals were detected by chemiluminescence using Pierce™ ECL Plus Western Blotting Substrate (Thermo Scientific) and autoradiography. Custom antibody for Bre1$^{1–645}$ was raised in rabbits by Thermo Scientific. Antibodies used are as follows with catalog numbers and source indicated in parentheses: anti-Flag M2 (F3165; Sigma); anti-Pgk1 (459250; Invitrogen); anti-Protein A (ab19483, Abcam); anti-V5 (R690-25, Invitrogen); anti-H2B (39237; Active Motif); anti-H3 (ab1791; Abcam); anti-H3K4me1 (39297; Active Motif); anti-H3K4me2 (39913; Active Motif); anti-H3K4me3 (39159; Active Motif); anti-mono- and polyubiquitinated conjugate monoclonal antibody (clone FK2) (BML-PW8810; Enzo Lifesciences); and anti-yeast UBC2/Rad6 (DZ33919; Boster Bio).

Co-immunoprecipitation

Log-phase cultures of yeast cells (50×10^7) expressing Flag epitope-tagged Rad6 or its mutants were harvested, washed once with PBS and stored at $–80°C$. Cells were lysed by bead beating after resuspension in IP-lysis buffer (10 mM Tris–HCl pH 8.0, 100 mM NaCl, 10% glycerol, 0.1% NP-40, protease inhibitors detailed above, and Roche cOmplete™ EDTA-free protease inhibitor cocktail). The samples were cooled on ice for 5 min between the bead beating cycles and clarified by two high-speed centrifugations (13 200 rpm at $4°C$) for 20 min and 10 min to obtain the final soluble lysate. Protein estimation was performed using Bio-Rad Protein Assay. An aliquot of the whole-cell lysate (50 μg) was set

aside for 'input'. Lysate (1 mg) from various yeast strains was used in immunoprecipitation with anti-Flag M2 magnetic beads (20 μl, Sigma) in a total volume of 1.5 ml made up with IP-lysis buffer and incubated with end-over-end rotation for 4 h at $4°C$. The beads were then washed four times with 1 ml of IP-lysis buffer and bead-bound proteins were eluted by boiling in $1\times$ Laemmli buffer (40 μl). Input and eluates were resolved by SDS–PAGE and subjected to western blotting with custom anti-Bre1 or anti-Flag M2 (Sigma) antibody.

Plasmid pTwist-EF1alpha or constructs 3V5-UBE2A-pTwist-EF1alpha or 3V5-UBE2A-P43L-pTwist-EF1alpha (3 μg) were transfected into Expi293F™ cells (Thermo Fisher Scientific) following the manufacturer's protocol. Two days after transfection, cells were harvested and lysates were prepared by sonication in IP-Lysis buffer (20 mM HEPES pH 8.0, 25% glycerol, 0.25% NP-40, 1.5 mM $MgCl_2$, 420 mM KCl, 0.2 mM EDTA, 0.5 mM DTT and protease inhibitors). An aliquot of the whole-cell lysate (50 μg) was set aside for 'input'. Lysates (1 mg) were used in immunoprecipitation with magnetic bead-conjugated anti-V5 rabbit monoclonal antibody (20 μl, Cell Signaling; Cat. No. #31628) in a total volume of 1.5 ml made up with IP-lysis buffer and incubated with end-over-end rotation for 4 h at $4°C$. The beads were then washed four times with 1 ml of IP-lysis buffer and bead-bound proteins were eluted by boiling in $1\times$ Laemmli buffer (40 μl). Input and eluates were resolved by SDS–PAGE and subjected to immunoblotting with anti-RNF20 (Cell Signaling, Cat. No. #11974) or anti-V5 (Invitrogen, Cat. No. R960-25) antibody.

Metal affinity co-purification

For co-expression, the coding sequences for His$_6$Rad6 or Bre1^{R6BR} or their mutant derivatives were inserted into pRSF-Duet (Novagen) and transformed into *E. coli* strain BL21-CodonPlus (DE3)-RIL (Agilent). A single colony for each construct was inoculated into 10 ml of LB medium supplemented with kanamycin (30 μg/ml) and chloramphenicol (10 μg/ml) and grown overnight at $37°C$ with shaking. The cultures were reinoculated at an $OD_{600 \, nm}$ of 0.1 in 50 ml of fresh LB medium supplemented with the antibiotics and grown at $37°C$ till an $OD_{600 \, nm}$ of 0.6. Cultures were induced with IPTG (0.25 mM) by growing them overnight at $16°C$. Aliquots for the cultures prior to and after IPTG induction were set aside. Next day, induced cultures (10 ml) were harvested by centrifugation at 6000 rpm for 10 min and cell pellets were stored at $–80°C$. Each cell pellet was resuspended in 1 ml of lysis buffer (25 mM Tris–HCl pH 7.9, 150 mM NaCl, 20 mM imidazole, 0.1% Triton X-100, 1 mM PMSF) and lysed by sonication for 1 min. The lysate was clarified by centrifugation at 12 000 rpm for 15 min. Aliquots from the lysate before and after centrifugation were set aside for the whole-cell lysate and soluble fraction, respectively. Triton X-100 (0.4%) was added to the clarified lysate (1 ml) prior to the addition of 50 μl of pre-equilibrated TALON® Superflow™ affinity resin (Cytiva) and incubation with end-over-end rotation at $4°C$ for 2 h. The beads were collected by centrifugation (3000 rpm for 3 min) and washed three times with the lysis buffer. The beads were boiled in $2\times$ SDS sample buffer to elute bound pro-

teins. The eluates and the various fractions set aside were resolved by 13% SDS–PAGE and stained using SimplyBlue™ SafeStain (Invitrogen). Following extensive destaining with water, the gels were scanned and protein bands were quantified by densitometry using ImageJ software.

Nucleosome reconstitution

Yeast octamers were produced using purified *S. cerevisiae* histones expressed in *E. coli* BL21-CodonPlus (DE3) RIL (41). Histones were purified from inclusion bodies and assembled into octamers by salt dialysis (42). Mononucleosomes were assembled by mixing equimolar amounts of purified histones and 180 bp sea urchin 5S rDNA using a linear salt gradient dialysis from 2 M to 50 mM KCl in a Slide-A-Lyser Mini Dialysis unit with a 7 kDa molecular weight cut-off (Thermo Scientific). The *5S* rDNA template was produced using PCR amplification with the following primers: 5SRDNA-FOR: 5′-AATTCCAACGAATAACTTCCA-3′ and 5SRDNA-REV: 5′-CCTGGCATACTAACCGAGCCC-3′. The 5SRDNA-FOR primer additionally contained Cy5 dye conjugated at its 5′ end. The amplified Cy5-labeled PCR product was purified by PEG–ethanol precipitation (42). The assembled mononucleosomes were separated from free DNA using 10–30% sucrose gradient sedimentation.

Gel shift assays

Increasing amounts of Rad6, Bre1[R6BR] or Rad6–Bre1[R6BR] were used along with mononucleosomes (100 nM) in gel shift assays, which were performed in a buffer containing 10 mM Tris–HCl pH 7.4, 50 mM KCl, 3 mM $MgCl_2$, 0.1 mg/ml bovine serum albumin (BSA), and with incubation at 30°C and gentle agitation (100 rpm) in a Thermomixer (Eppendorf) for 30 min. The reactions were mixed with an equal amount of 10% glycerol and resolved in a native 4% polyacrylamide gel made from a 37.5:1 acrylamide:bisacrylamide mix. The gel was equilibrated in 0.5× TBE for 1 h before loading the samples. Electrophoresis was then performed for 2 h at a constant voltage (80 V). Gels were scanned on a Typhoon Trio (Amersham Biosciences) at 633 nm. Gel shift assays were performed with increasing amounts of Rad6–Bre1[R6BR], rad6-P43L–Bre1[R6BR] or rad6-P47T–Bre1[R6BR] essentially as described above. The fraction of the nucleosome-bound wild-type- or mutant Rad6-containing complexes was quantified from gel scans. Equilibrium dissociation constants (K_d) were determined in GraphPad Prism using the non-linear least square fitting function and the specific binding with Hill slope setting for various concentrations of wild-type or mutant Rad6–Bre1[R6BR] complexes versus their fraction bound to nucleosomes.

In vitro ubiquitination assay

The ubiquitination reaction was performed for 2 h at 30°C essentially as reported previously (43) and in 1× reaction buffer and 5 mM Mg-ATP (Ubiquitylation Assay Kit, Catalog No. ab139467; Abcam), 0.1 μM recombinant yeast glutathione *S*-transferase (GST)–Uba1 (E1, R&D Systems), ubiquitin (2.5 μM; R&D Systems), 0.2 μM recombinant wild-type or mutant Rad6 alone or in complex with full-length Bre1 or Bre1[R6BR], and 2 μM recombinant yeast histone H2B or mononucleosome (substrate). The reactions were stopped by adding 2× Laemmli sample buffer (Bio-Rad) and resolved by 12% SDS–PAGE prior to immunoblotting using the following antibodies as detailed above: anti-mono- and polyubiquitinated proteins antibody (clone FK2), anti-yeast H2B, anti-H3, anti-Rad6 or anti-Bre1.

Biolayer interferometry (BLI)

Data were collected using an Octet® RED96 system and processed with Octet Data Analysis software version 8.1 (Forte Bio). Biotinylated Bre1[R6BR] was immobilized over High Precision Streptavidin (SAX) Biosensors (ForteBio) as the ligand (100 nM). His6Rad6 or its mutants were used as the analyte. Protein concentrations were determined using a NanoDrop UV-Vis Spectrophotometer (280 nm). The buffer for interaction experiments comprised 1× PBS pH 7.4, 1 mM DTT, 1% BSA (Sigma) and 0.02% Tween-20 (Sigma). Biotinylated Bre1[R6BR]-bound Biosensor chips were dipped in various concentrations of the analyte to measure association and transferred back to buffer wells for monitoring dissociation. For quantitation, five or six concentrations of the analyte were used, and the exact concentration was varied depending on the affinity of the specific analyte–ligand combination. A global fit (or full) with simultaneous, constrained fit of all eight sensorgrams was used for data analysis. The reported kinetic rate constants (k_a and k_d) were determined from the fit of a 1:1 binding model. Two biological independent protein expression and purifications, and three independent technical replicate experiments were performed.

SEC-MALS

SEC-MALS (multi-angle light scattering) was performed using a Superdex 200 Increase 10/300 GL size exclusion column (Cytiva) on a Bio-Rad NGC Chromatography system coupled to inline static light scattering (Dawn, Wyatt Technology), differential refractive index (Optilab, Wyatt Technology) and UV detection. Purified proteins were diluted to 2 mg/ml in running buffer (25 mM Tris–HCl pH 7.5, 150 mM NaCl, 5% glycerol, 1 mM TCEP) and 55 μl of each sample was run at a flow rate of 0.5 ml/min at 25°C. All proteins eluted as single peaks, shown in Supplementary Figure S4. Data were analyzed using ASTRA software (Wyatt Technologies). The exported UV, elution volumes and molar mass data were used to plot the graphs in MS Excel.

RNA-seq

Total RNA was isolated using the acid-phenol method. Yeast cells were grown to $OD_{600\,nm}$ 0.7 and harvested (10.5×10^7), washed with RNase-free water and stored at –80°C. Frozen cells were resuspended in 0.3 ml of TES buffer (10 mM Tris–HCl pH 7.5, 10 mM EDTA, 0.5% SDS), combined with an equal volume of phenol pH 4.3 (Thermo Scientific) and incubated at 65°C for 1 h with agitation (140 rpm) in a Thermomixer (Eppendorf). The lysate

was cooled on ice for 10 min and centrifuged (13 200 rpm, 10 min at 4°C). Supernatant (0.25 ml) was combined with an equal volume of 25:24:1 phenol–chloroform–isoamyl alcohol pH 4.3 (Thermo Scientific), mixed well by vortexing and end-over-end rotation for 10 min at 4°C, and centrifuged (13 200 rpm, 10 min at 4°C). Supernatant (0.2 ml) was overlaid onto 0.8 ml of 5.7 M CsCl (Sigma) and centrifuged in a Beckman Optima Tabletop Ultracentrifuge with an MLA-130 rotor (30 000 rpm, 18 h at 4°C). The pellet was dissolved in 0.2 ml of RNase-free TE pH 7.0 (Ambion) by incubating for 1 h at 4°C, before precipitation using ethanol and sodium acetate pH 4.3 (Ambion), and centrifuged (13 200 rpm, 20 min at 4°C). The pellet was washed with 70% ethanol, dried and dissolved in $0.1 \times$ TE. An equal amount of RNA (50 μg) was further purified using the Qiagen RNeasy Mini Kit by following the manufacturer's recommendations. Purified RNA was used in library preparation with the Illumina TruSeq HT Stranded mRNA Library Preparation Kit with poly(A) selection. For RNA isolated from strains DHY217 and YMC203, the Illumina TruSeq Stranded Total RNA with Ribo-Zero Gold rRNA Removal Kit Yeast was used. The libraries were subjected to 50 bp single-read sequencing in HiSeq 2500. Three independent RNA isolates from each yeast strain were sequenced.

qChIP-seq or ChIP-Rx

Saccharomyces cerevisiae strain YZS375 transformed with pMC6-based constructs to express either Rad6-3V5 or the mutants (rad6-P43L-3V5, rad6-E49K-3V5 or rad6-P47T-3V5) or strain YZS413 (*bre1Δ*) transformed with vector pRS315 were grown in -TRP medium to mid-log phase and cross-linked with 1% formaldehyde (Sigma) for 20 min at room temperature. Cross-linking of cells was stopped by adding glycine (0.125 M) and washing once with PBS. Multiple aliquots of 100×10^7 cross-linked cells were harvested. For the reference genome, *C. glabrata* transformed with pMC8 was grown in YPAD medium supplemented with cloNAT (100 μg/ml), subjected to formaldehyde cross-linking as described above, and aliquots of 20×10^7 cells were harvested. Cross-linked *S. cerevisiae* (100×10^7) and *C. glabrata* (20×10^7) cells were combined prior to spheroplasting, followed by isolation of nuclei and chromatin preparation as previously described. Briefly, nuclei were resuspended in FA140 buffer (50 mM HEPES-KOH, pH 7.5, 140 mM NaCl, 1 mM EDTA, 1% Triton X-100, 0.1% sodium deoxycholate, 140 mM NaCl) and sonicated in Diagenode Bioruptor® Pico for 30 min (60 cycles of 30 s ON and 30 s OFF). After centrifugation (13 200 rpm, 15 min at 4°C), an aliquot of the dialysate (25 μl) was set aside for isolating input DNA. Prior to immunoprecipitation, chromatin was pre-cleared with 50 μl of Protein A or Protein G Dynabeads (Invitrogen) blocked with BSA and fish skin gelatin. Pre-cleared chromatin was then combined with custom Bre1 antibody or anti-V5 (15 μl; Bio-Rad, Cat. No. MCA1360) antibody and incubated overnight at 4°C with end-over-end rotation. The immune complex was captured by adding 50 μl of Protein A or Protein G Dynabeads and incubating for an additional 2.5 h. Bead-bound complexes were then washed sequentially for 5 min each with end-over-end rotation at 4°C with FA buffer + 140 mM NaCl (three

washes), FA buffer + 1000 mM NaCl (two washes), FA buffer + 500 mM NaCl (two washes) and one wash each with LiCl/NP-40 buffer (10 mM Tris–HCl, pH 8.0, 250 mM LiCl, 0.5% NP-40, 0.5% sodium deoxycholate) and TE (10 mM Tris–HCl, pH 8.0, 1 mM EDTA). Elution, reverse cross-linking of ChIP and input DNA, and enzymatic digestion to remove RNA or protein were performed as described (39). Library construction was performed using NEBNext Multiplex Oligos (Index Primers Set 1) and the NEBNext ChIP-seq Library Prep Reagent Set for Illumina prior to 50 bp single-end sequencing using Illumina Hiseq2500. Two biological replicates were performed for each strain.

Bioinformatics

Illumina sequencing reads were aligned to the *S. cerevisiae* genome (SGD release R64, UCSC SacCer3) using STAR (version 2.6.1, Dobin reference). Gene counts were generated using Subread featureCounts (version 1.6.3, reference) employing a custom gene reference that included untranslated regions (UTRs) and lacked dubious ORFs. Multimapping alignments were not counted. Differential gene expression analysis was performed using the R package DESeq2 (version 1.20, http://genomebiology.com/2010/11/10/R106). Genes passing two thresholds, an adjusted *P*-value of <0.05 and an absolute $\log_2$ ratio of 0.585 (i.e. 1.5-fold change), were considered differentially expressed and used in subsequent analysis. Read-depth normalized coverage was used for visualization in a genome browser to confirm changes in expression. Gene Ontologies were determined using the Gene Ontology Term Finder available at the Saccharomyces Genome Database (SGD). Total counts, gene lists and other relevant metrics associated with the RNA-seq analysis are included in the Supplementary Dataset.

For ChIP-Rx, sequence reads were aligned independently to both the *C. glabrata* (Ensembl Fungi release 30, GCA_000002545.2) and *S. cerevisiae* (Sac-Cer3) genomes. Alignments were assigned to species of origin using the script cross_species_alignment_picker (https://github.com/tjparnell/HCI-Scripts). A normalization factor for the reference genome was calculated as $1/(\text{Count}_{\text{glabrata}}/1e^6)$ (44). Depth-normalized fragment coverage, $\log_2$ fold enrichment and q-value tracks were generated using the MultiRepMacsChIPSeq package (version 11, https://github.com/HuntsmanCancerInstitute/MultiRepMacsChIPSeq), a wrapper for processing multiple samples and replicates using the Macs2 ChIPSeq software. Options to the pipeline included the *Candida* normalization factors, a fragment extension size of 150 bp and a maximum duplicate depth of 1. Replicates were averaged together after depth normalization. A blacklist of regions to exclude from analysis included regions of high copy number, including mtDNA, rDNA and subtelomeric loci. High enrichment was obtained at Pol III genes with the Bre1 antibody even in the *bre1Δ* strain, indicating an unwanted cross-reactivity (Supplementary Figure S17). Therefore, tRNA, *SCR1* and *RPR1* genes were also included in the blacklist and excluded from analysis.

ChIP enrichment data were collected over genes using applications from the BioToolBox package (https://github.
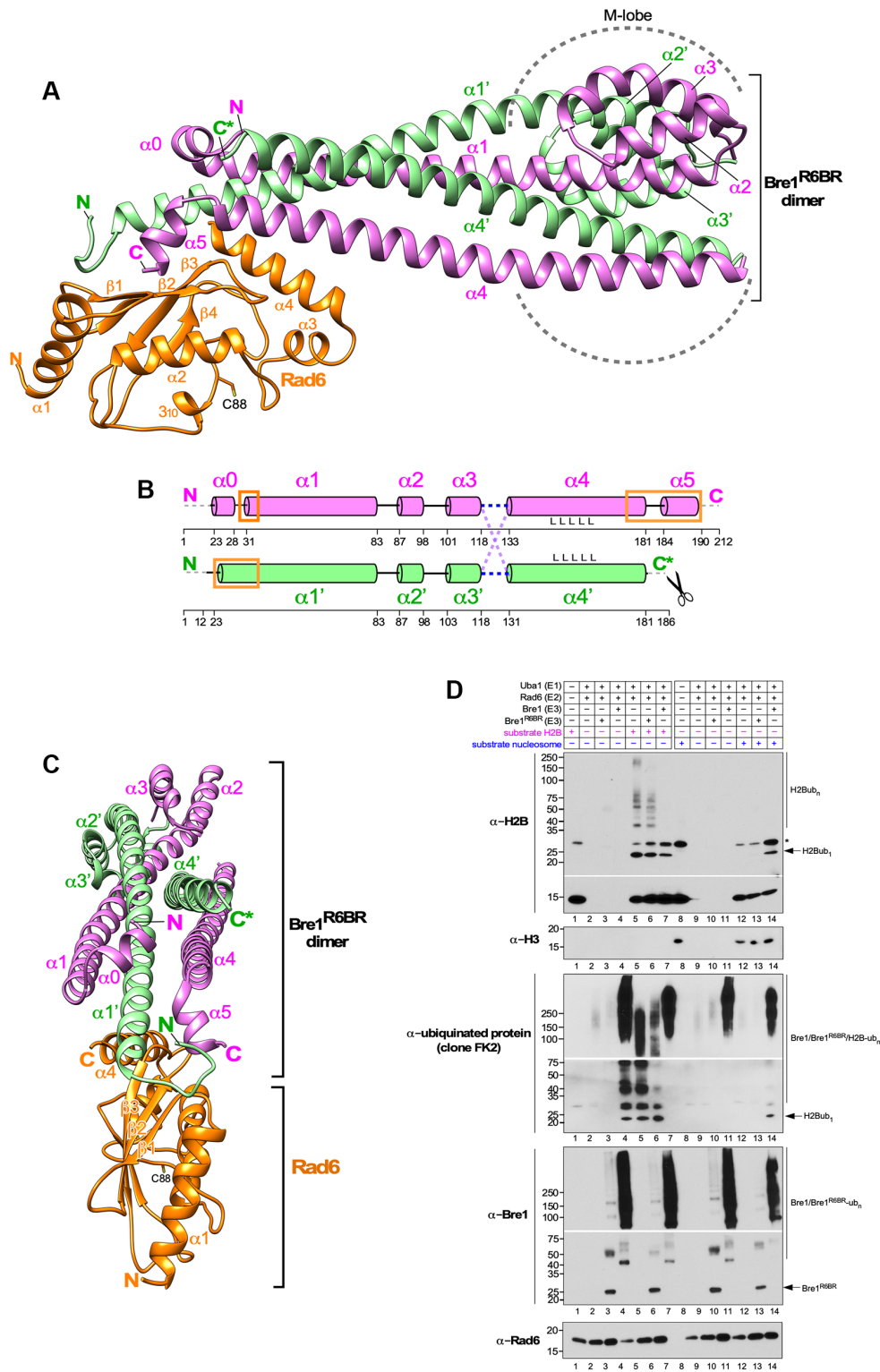
Figure 1. Crystal structure of Rad6 bound to the asymmetric Bre1[R6BR] dimer and their *in vitro* ubiquitination activity. (**A**) Gray dotted lines encompass the eight-helix bundle or the M-lobe. *C** denotes the protease-sensitive C-terminal end of one Bre1[R6BR] subunit. (**B**) Schematic representation of the Bre1[R6BR] dimer. Helices are shown as cylinders. Unstructured regions are shown as dotted gray lines. The possible connections between α3 and α4 helices are indicated by the colored dotted lines (see Supplementary Figure S6). The simpler side-on connectivity model (blue dotted line) is adopted for illustrative purposes. Regions of Bre1 that contact Rad6 are indicated by orange rectangles. The scissors indicate the protease processing of one Bre1[R6BR] subunit. (**C**) Side view. (**D**) *In vitro* ubiquitination assay. Substrate (recombinant yeast H2B, pink or reconstituted yeast nucleosome, blue) was incubated with yeast Uba1 (E1), Rad6 (E2) and either full-length Bre1 or Bre1[R6BR] (E3) along with Mg^{2+} and ATP. The presence or absence of an indicated protein is indicated by + or –, respectively. Size markers and auto-ubiquitinated Bre1 or Bre1[R6BR] species are indicated. Blots were probed with the stated antibodies. Histone H3 serves as a control for nucleosomes.
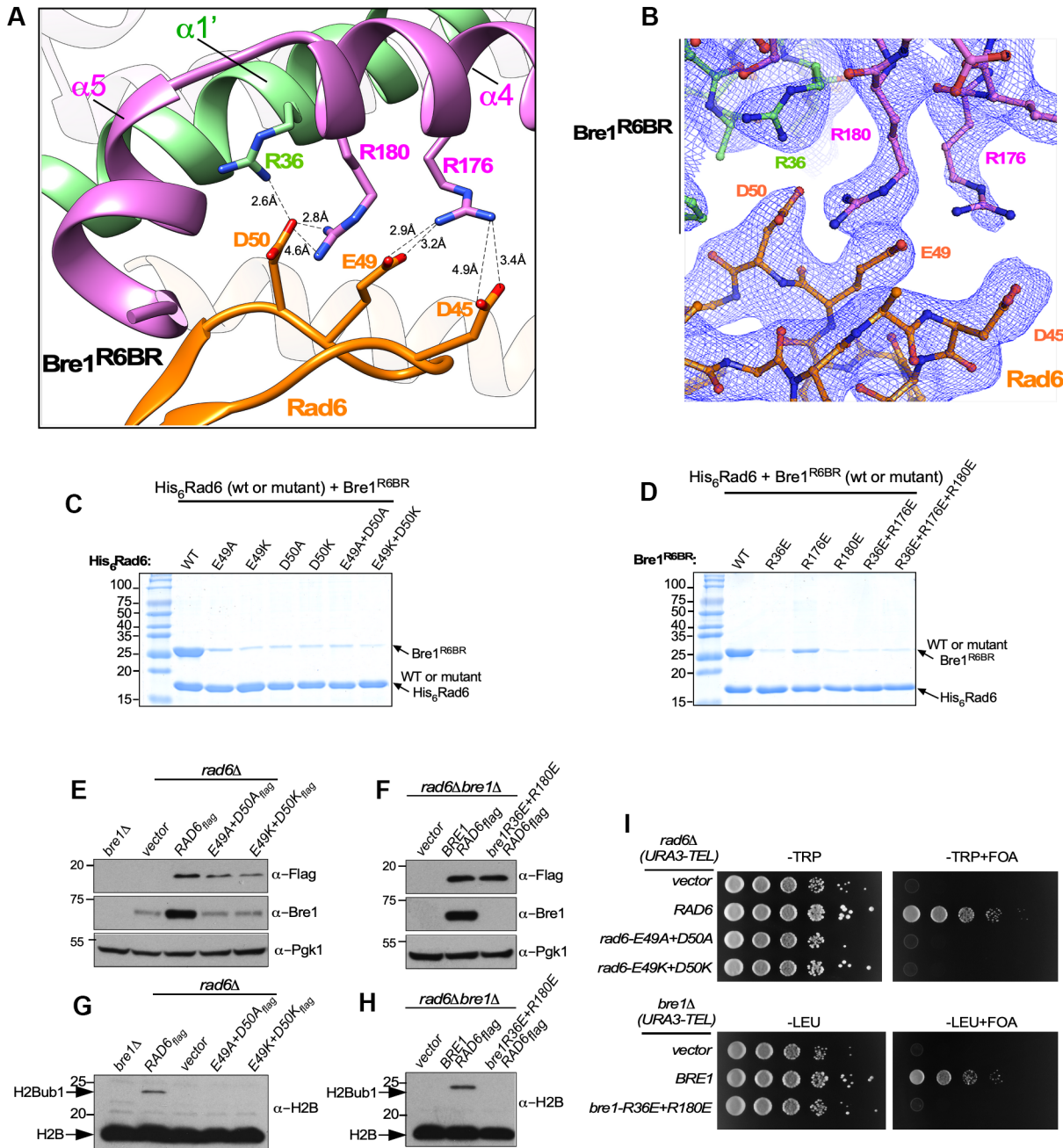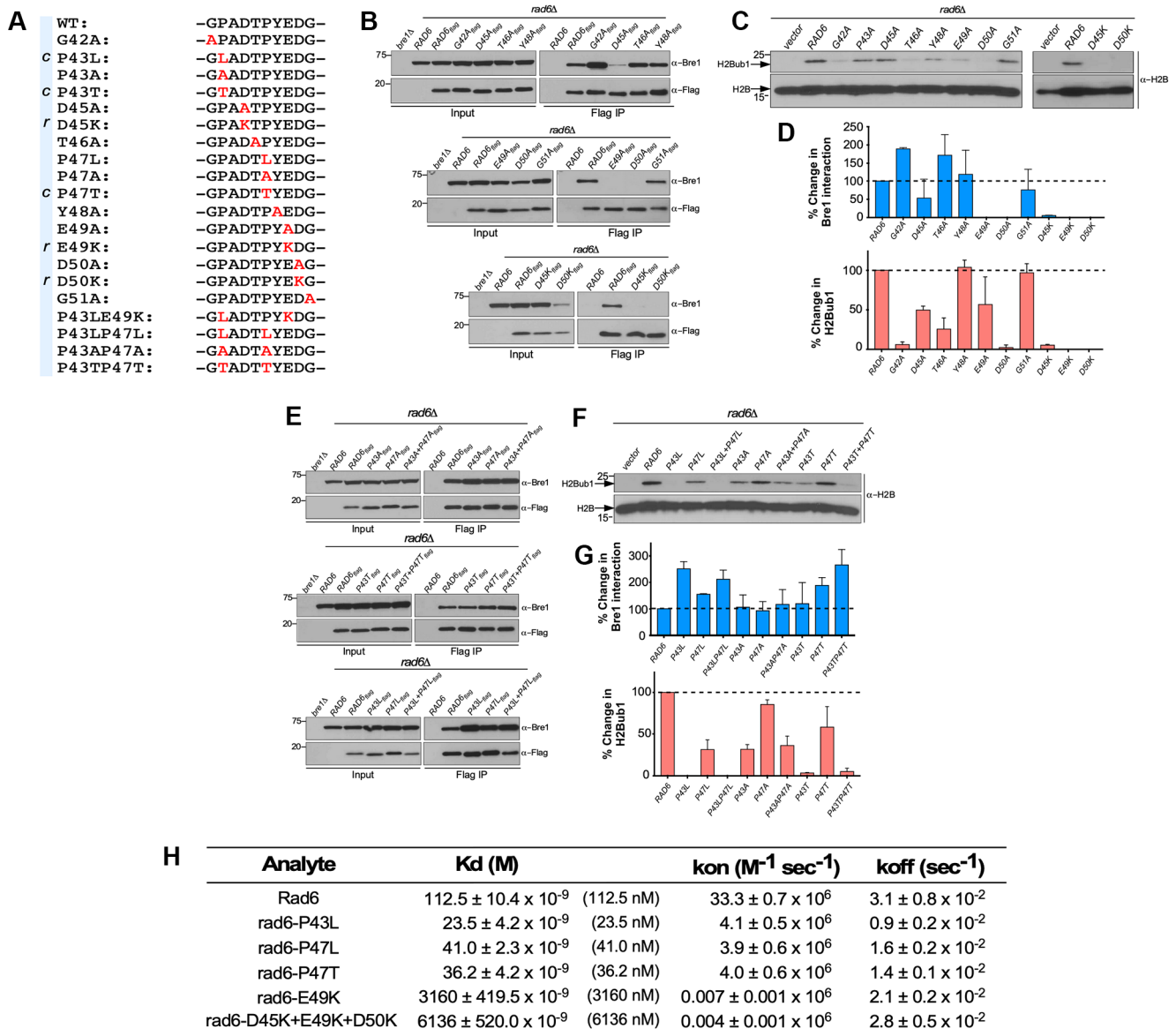
Figure 2. The Rad6–Bre1 crystallographic interface is important for binding, H2Bub1 abundance and gene silencing. (**A**) Electrostatic interactions of Bre1 R36, R176 and R180 with Rad6 E49 and D50. Rad6 D45 approaching Bre1 R176 is also shown. (**B**) The $2F_o–F_c$ electron density map is shown as blue mesh for the residues of the Rad6–Bre1^{R6BR} complex contoured at 1.0σ. (**C** and **D**) SDS–PAGE analysis of metal affinity co-purification of wild-type and interface mutant Rad6 or Bre1. (**E–H**) Immunoblots showing steady-state levels of H2Bub1, Flag-tagged Rad6 or its mutants and Bre1 or its mutants. Pgk1 levels serve as a loading control. (**I**) Interaction interface mutations in Rad6 or Bre1 disrupt the telomeric silencing of *URA3*.

com/tjparnell/biotoolbox). Plots were generated using gg-plot and pheatmap packages in R and GraphPad Prism.

Molecular docking

The coordinates for the yeast nucleosome (PDB ID: 1ID3) and Rad6–Bre1^{R6BR} (PDB ID: 7UV8) were processed using the protein preparation function in Molecular Operating Environment (MOE) software. Hydrogen atoms and partial charges were then added by the program. Protonation was then assigned using the recommended default settings. Models for the Rad6–Bre1^{R6BR} complex docked onto the nucleosome were obtained using the protein–protein dock tool in MOE. Docking was initiated with a coarse-grained (CG) model that reduced the computational search space. Exhaustive sampling was then carried out to create a set of initial poses. The Hopf fibration was used to generate a set of uniformly distributed rotations (45), and a fast

Figure 3. The backside loop-3 of Rad6 at the crystallographic interface is important for Rad6–Bre1 binding dynamics, H2Bub1 abundance and gene silencing. (**A**) The amino acid sequence of the Rad6 backside loop and the introduced mutation are shown. *c*, cancer-relevant mutation in the human Rad6 homologs UBE2A or UBE2B, as listed in the Catalogue of Somatic Mutations in Cancer (COSMIC) database; *r*, charge-reversal mutation. (**B** and **E**) Immunoblots showing the co-immunoprecipitation (Flag IP) of Rad6 or its indicated mutants with Bre1. (**C** and **F**) The steady-state levels of histone H2BK123 ubiquitination (H2Bub1) in the *rad6Δ* null strain or expressing either wild-type Rad6 or the indicated loop mutation. (**D** and **G**) Sections of the blot with H2Bub1 and H2B were probed with different concentrations of the anti-H2B antibody. Quantitation from at least two independent co-immunoprecipitation and immunoblot experiments as shown in (B, C) or (C, F). Co-precipitating Bre1 levels were normalized to their respective Rad6 levels. H2Bub1 levels were normalized to their respective H2B levels. Change in normalized Bre1 or H2Bub1 levels in a mutant is shown relative to that in the wild type, which was set as 100% (dotted line). Error bars, standard deviation from the mean. (**H**) Binding constants determined using BLI. Values were calculated from two biological and three technical replicate experiments and using a 1:1 global fitting (Supplementary Figure S17).

Fourier transform (FFT) was used to sample all translations for a given rotation. This generated a set of initial docked poses of the models, which were then filtered based on restraints and further subjected to coarse refinement. The refined model poses were then converted back to all atom models, which were refined with side chain packing and molecular mechanics minimization to produce a list of all atom protein–protein docked poses. Approximately 100 co-ordinates were developed according to the free binding energy of the complex (ΔG) and rescored using the GVI/WSA function in MOE, which adds an empirical term to the solvation free energy using GBVI. The best five docked complexes with low $-\Delta G$ value were selected. Among these five models, the one shown in Figure 4A had Rad6 correctly oriented with its active site Cys88 in close proximity (7.5 Å) to histone H2B Lys123, the site of ubiquitination.
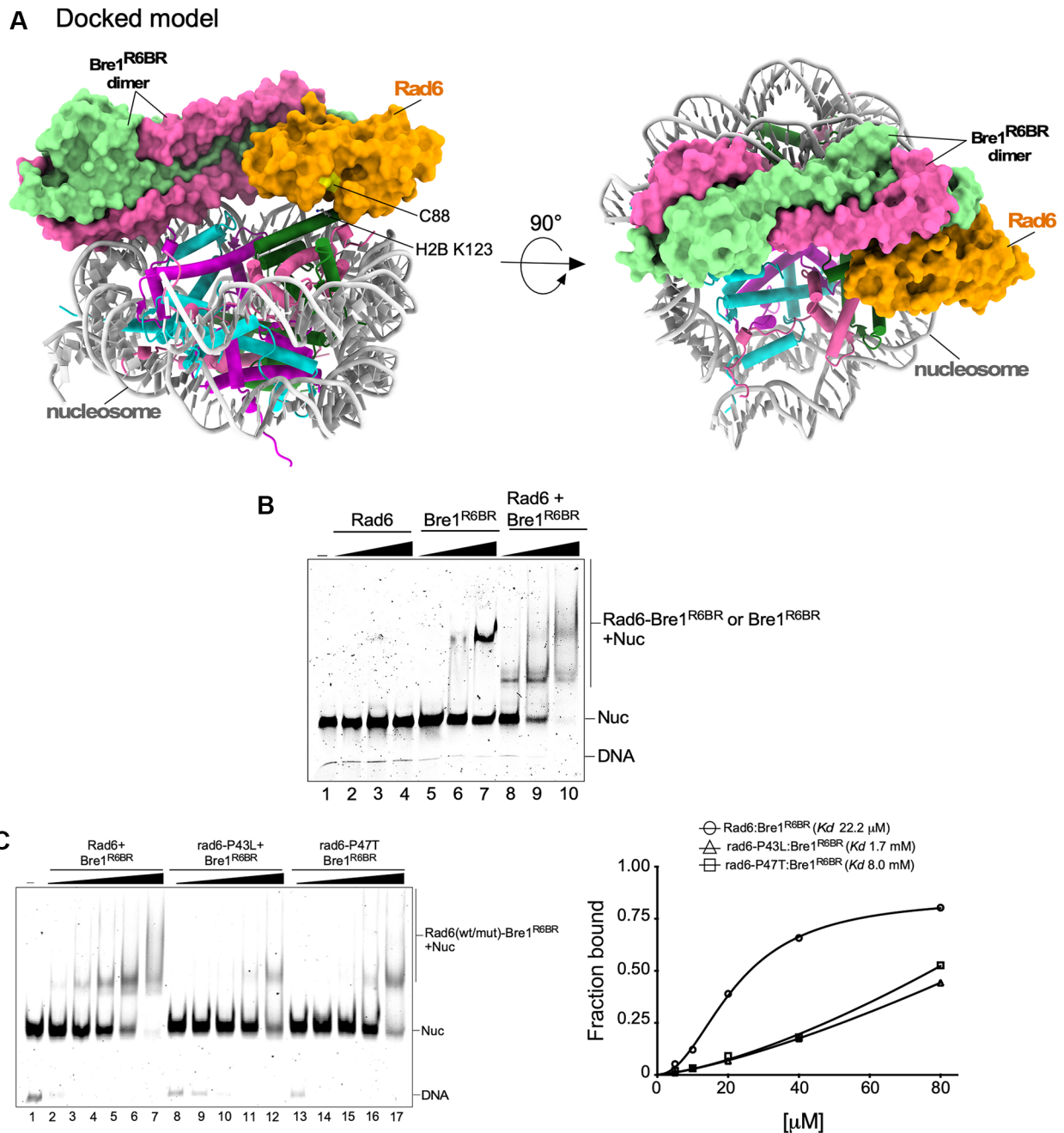
Figure 4. Rad6–Bre1^{R6BR} binds nucleosome. (**A**) Molecular docking of Rad6–Bre1^{R6BR} with yeast nucleosome. (**B** and **C**) EMSAs. Increasing amounts of recombinant Rad6 or Bre1^{R6BR} alone or either wild-type or the indicated proline mutant Rad6 bound to Bre1^{1R6BR} (20, 40 or 80 μM) were incubated with *in vitro* reconstituted yeast mononucleosomes (Nuc) (100 nM). Protein complexes were resolved by native gel electrophoresis prior to imaging. A representative gel image from at least three independent nucleosome binding experiments is shown. Binding isotherm curves for wild-type or mutant complexes with yeast nucleosome are shown. The plot shows the average of four independent experiments, and computed affinity constants are indicated.

RESULTS

Silencing-defective Rad6 mutations alter Bre1 binding

Rad6 associates with various E3 ubiquitin ligases to function in transcription, DNA repair and protein degradation (13,46–48). Over two decades ago, it was reported that *rad6-P43L* and *rad6-E49K* alleles impair telomeric silencing (Supplementary Figure S1a); but they retain nearly complete activity in protein degradation and DNA repair (49).

This observation prompted us to hypothesize that these mutations might disrupt interactions with the Bre1 E3 ligase, which is required for H2B K123 monoubiquitination (13,14) and hence for histone H3K4 trimethylation (me3), which in turn is important for telomeric silencing (50,51). Consistent with this possibility, we found that the steady-state levels of H2Bub1 and H3K4me3 were reduced in *rad6-P43L* and *rad6-E49K* mutants (Supplementary Figure S1b–d). Collectively, these observations indicate that *rad6-P43L*

and/or *rad6-E49K* are impaired in their ability to perform H2Bub1.

In support of the model that the reduced H2Bub1 in these mutants is a result of defects in their binding to Bre1, co-immunoprecipitation (co-IP) experiments showed that rad6-E49K and rad6-P43LE49K proteins did not associate with Bre1 (Supplementary Figure S2a). The P43L mutation is found in human Rad6 (UBE2A) in cancers ([52]), and co-IP showed enhanced binding of UBE2A-P43L to RNF20 (the Bre1 homolog) (Supplementary Figure S2b). The yeast rad6-P43L also showed enhanced Bre1 interaction despite being defective in H2Bub1 (Supplementary Figures S1b, c, 2a). The N-terminal Bre1 residues 1–212 were previously reported to be necessary and sufficient to interact with Rad6 *in vitro* ([16,17]). To further verify our observations from co-IP experiments, we co-expressed in bacteria a hexahistidine (His$_6$)-tagged Rad6 (wild type or mutant) with the N-terminal Rad6-binding region (R6BR) region of Bre1 (residues 1–212). Consistent with the co-IP results, affinity purification showed that Rad6-E49K displayed impaired Bre1 binding whereas Rad6-P43L protein showed enhanced Bre1 binding (Supplementary Figure S2c). These observations indicate that Rad6 residues P43 and E49 contribute to its physical interaction with the Bre1 E3 ligase *in vivo* and *in vitro*.

Overall structure of the Rad6–Bre1^{R6BR} complex

We were able to co-express and co-purify a Rad6–Bre1^{R6BR} complex in an apparent 1:2 subunit stoichiometry from bacteria (Supplementary Figure S3a), which was further confirmed by SEC-MALS (Supplementary Figure S4). Crystallization of the Rad6–Bre1^{R6BR} complex was facilitated by reductive methylation and partial proteolysis (Supplementary Figure S3, Materials and Methods). The purified complex and crystals appeared to include approximately equal amounts (by SDS–PAGE) of a full-length and a truncated Bre1^{R6BR} (Supplementary Figure S3a, c). MS indicated that the truncated Bre1^{R6BR} lacked the C-terminal residues 187–212 (Supplementary Figure S3b), suggesting that Bre1 can form an asymmetric dimer when bound to Rad6.

Co-crystal structure confirmed this possibility, revealing an asymmetric dimer of Bre1^{R6BR} bound to one Rad6 subunit at its 'backside', 30 Å distant from the catalytic cysteine (C88) (Figure 1A–C; Supplementary Table S1). Each Bre1^{R6BR} monomer comprises a long N-terminal helix (α1), two short helices (α2 and α3) and a long C-terminal helix (α4) (Figure 1A–C). The two Bre1^{R6BR} subunits form an elongated dimer that has overall dimensions of ~100 Å × 30 Å × 30 Å. The subunits associate through lengthwise packing of α1/1′ and α4/4′ and folding with α2/2′–α3/3′ into an eight-helical bundle (M-lobe) at one end of the elongated molecule (Figure 1A; Supplementary Figure S5). Short additional helices, α0 and α5, are found at the N- and C-termini of the longer subunit near the Rad6–Bre1 interface (Figure 1A–C).

Residues lacking clear density were omitted from the structural model including the N-terminal 20 residues in the Bre1^{R6BR} subunits; the C-terminal 11 residues of the longer (non-proteolyzed) Bre1^{R6BR} subunit and residues 121–130 in the connection between α3/3′ and α4/4′ helices also lack

density in both subunits (Figure 1A, C; Supplementary Figure S6a). Consequently, there are two possible ways of connecting α3 and α4 (Supplementary Figure S6b–g). For illustrative purposes, we assume the simpler 'side-on' connectivity model, in which Rad6 contacts are mediated primarily by α1′ from the proteolyzed Bre1^{R6BR} subunit and α4 from the full-length Bre1^{R6BR} subunit.

An asymmetric Bre1^{R6BR} homodimer binds one Rad6

The structure shows that the Bre1^{R6BR} M-lobe is two-fold symmetric about an axis that aligns approximately with the long dimension of Bre1 while the elongated region, comprised of α1/1′ and α4/4′, displays asymmetry (Figure 1A–C). Most of α1 and α1′ pack parallel against each other in a largely coiled-coil-like manner, as do α4 and α4′, which contain a canonical leucine repeat (Figure 1B; Supplementary Figure S5c). In contrast, packing between the α1/1′ and α4/4′ pairs creates an asymmetric Bre1 dimer that binds to a Rad6 molecule near the N-termini of α1 and α1′, and the C-terminal portions of α4 and α5 (Figure 1A–C; Supplementary Figure S5a).

The asymmetric disposition of the Bre1^{R6BR} C-termini, in which α4 and α5 contact Rad6 while α4′ is more solvent exposed, explains the differential sensitivity to proteolysis (Supplementary Figure S3). The asymmetry is also pronounced at the N-termini, where residues near the N-termini of α1 and α1′ both contact Rad6, but α1′ extends for an additional two turns and more N-terminal residues adopt distinct conformations (Figure 1A–C). Interestingly, many species, including *Schizosaccharomyces pombe* and humans, express two distinct Bre1 homologs ([15,18,53]), which may correspond to the two structurally distinct subunits of the Bre1 homodimer.

Similarities and differences of Rad6–Bre1^{R6BR} relative to other E2–E3 complexes

Multiple studies have identified the 'backside' surface of E2 enzymes as an important site of regulatory interaction, including the non-covalent binding of ubiquitin to the E2 Ube2D3 ([54]) and interactions of other E2s with E3 ligases (Rad18, gp78 and Ubr1) and an E2 activator (Cue1) ([55–57]). While Bre1^{R6BR} is considerably larger than other reported structures of E2 backside binders, it buries a modest (815 Å^2) surface area and differs from all other reported E2 backside-binding partners in being dimeric (Supplementary Figure S7). Comparison with a recently reported structure for the Rad6–Ubr1 complex ([57]) shows that Bre1 α1′ overlaps with a backside-interacting helix in Ubr1 (Supplementary Figure S8), although these overlapping helices are in an antiparallel orientation. The Rad6–Bre1^{RBR} interface is distinct from other reported E2 complex structures, with the closest similarity between the central portion of Bre1 α1′ and helices of gp78–G2BR and Cue1–U7BR that contact their partner E2s UBE2G2 and Ubc7, respectively (Supplementary Figure S8). Structural overlaps reveal a well-conserved interaction between a positively charged arginine or lysine residue in the E3 helices and a negatively charged aspartate or glutamate in loop-3 at the E2 backside (Supplementary Figure S9a–c). Nevertheless, even these examples

differ considerably, with the second helix (α4) being unique to Rad6–Bre1^{R6BR} (Supplementary Figure S9d).

Bre1^{R6BR} alters the activity of Rad6

The backside binding of E3 ligases regulates both structure and catalytic activities of their partner E2 enzymes (56,58–59). We therefore superposed the Rad6–Bre1^{R6BR} structure with that of free Rad6 (60) or the Rad6–ubiquitin thioester mimic (61) (Supplementary Figure S10). Consistent with the finding that Bre1^{R6BR} is sufficient for Rad6 activation (17), Rad6–Bre1^{R6BR} overlapped closely with the 'ubiquitin-charged' or enzymatically active Rad6 [root mean square deviation (RMSD) ∼0.65 Å] (Supplementary Figure S10b). While the RMSD on all backbone Cα atoms between Rad6–Bre1^{R6BR} and free Rad6 was 0.68 Å, residues 90–95 in a loop at the opening of the active site and residues 116–120 at the active site cleft showed a deviation of 1.08 Å and 1.95 Å, respectively (Supplementary Figure S10a). Residues in these flexible segments have well-documented roles in regulating the catalytic functions of E2 enzymes: Q93 in human Rad6 or H94 in UBE2G2 maintain the catalytic microenvironment essential for substrate lysine deprotonation (62,63), and the 'gateway residue' S120 in the active site cleft of yeast and human Rad6 regulates enzymatic activity including formation or levels of H2Bub1 *in vitro* or *in vivo* (64–66). Thus, our results indicate that the backside binding of Bre1^{R6BR} does not alter the overall fold of Rad6 but induces changes around the active site that could potentially affect its catalytic functions.

To test this possibility, we examined the impact of Bre1^{R6BR} binding on Rad6's enzymatic activity by assaying Rad6-mediated polyubiquitination of histone H2B *in vitro* (67,68). This robust *in vitro* ubiquitin chain-forming activity of free Rad6 was prevented when associated with full-length Bre1 and was reduced when associated with Bre1^{R6BR} (Figure 1D). We also found that neither Rad6 nor Rad6–Bre1^{R6BR} catalyzed the robust histone H2B monoubiquitination on a nucleosomal substrate as obtained using Rad6–Bre1 (Figure 1D). Thus, binding of Bre1^{R6BR} restricts the polyubiquitination activity of Rad6, but is insufficient to support monoubiquitination of histone H2B on a nucleosome. These observations with Bre1^{R6BR} differ from the ubiquitin chain-promoting activities of the E2 backside binders gp78–G2BR (59) and Cue1–U7BR (69) but are similar to AO7–U5BR (70) and Rad18–R6BD (71), which limit the ubiquitination activity of their cognate E2s.

The Rad6–Bre1^{R6BR} interaction interface is required for H2Bub1 functions

The 815 Å^2 Rad6–Bre1^{R6BR} interaction surface comprises multiple residues close to the N- and C-termini of the Bre1^{R6BR} dimer and those at Rad6's backside, including P43 and E49 (Supplementary Figure S11a, b), which were implicated in our genetic and binding studies (above). Distinctive features of the interaction include: (i) interactions of Rad6 E49 and D50 with Bre1's R36, R176 and R180 (Figure 2A); (ii) interactions of Rad6 W149 and E150 with Bre1's K31, which was previously implicated in Rad6–Bre1 interaction

(17) (Supplementary Figure S11c); and (iii) multiple interface residues are conserved from yeast to human, including Rad6 P43, E49 and D50 (Supplementary Figure S12a).

To validate the crystal structure, we mutated residues at the Rad6–Bre1^{R6BR} interaction interface (Figure 2A, B). Consistent with the structure, charge neutralization or reversal substitutions at Rad6 E49 and D50 or Bre1 R36, R176 and R180 disrupted co-purification in pull-down experiments (Figure 2C, D; Supplementary Figure S13). Consistent with Rad6 association stabilizing Bre1 *in vivo* (72), we found that steady-state Bre1 levels were severely reduced in the absence of Rad6, but not in the presence of its catalytically dead mutant (rad6-C88A) (Supplementary Figure S14). Moreover, mutations in Rad6 E49 and D50 or Bre1 R36 and R180 that disrupt the Rad6–Bre1 interaction also decreased Bre1 levels *in vivo* (Figure 2E, F). This indicates that residues at the crystallographic interface are important for Rad6–Bre1 binding in solution and for *in vivo* stability of Bre1. Additionally, mutation of Rad6–Bre1 interface residues decreased or abolished H2Bub1 (Figure 2G, H) and caused silencing defects (Figure 2I). These observations validate the functional relevance of the crystallographic interface (Figure 2A, B) and demonstrate that the interacting residues are crucial for Rad6–Bre1 *in vivo* association and function.

Mutations in loop-3 of Rad6 alter the Rad6–Bre1 interaction dynamics

Rad6 interface residues E49 and D50 are part of the evolutionarily conserved loop-3 at the backside of Rad6 and its homologs (Supplementary Figure S12a) and E2 enzymes in general. Loop-3 also includes P43, whose leucine substitution resulted in increased Bre1 binding but decreased H2Bub1 levels *in vivo* (Supplementary Figure S12). From the structure, it is evident that loop-3 lies at the Rad6–Bre1^{R6BR} interaction interface (Supplementary Figure S12b) and thus it could impact Rad6–Bre1 binding and associated biological functions. To test this possibility, we performed comprehensive mutagenesis of the loop-3 residues via alanine or charge reversal substitutions either singly or in combination (Figure 3A). We also found P43L and P47T mutations in loop-3 of human Rad6 homologs in cancers following a query of the COSMIC database (52). Therefore, either single or combinatorial leucine or threonine substitutions were introduced at P43 and P47 of yeast Rad6. We then examined the effects of these mutations on Rad6–Bre1 interaction and their *in vivo* biological functions including histone H2B monoubiquitination and gene silencing.

Bre1 interaction was altered, steady-state H2Bub1 levels were decreased and a silencing defect that ranged from mild to severe was observed for mutation at other Rad6 loop-3 residues in addition to E49 and D50 (Figure 3B–D; Supplementary Figure S15). Of note, mutation of the interface residue Rad6 D45 adversely affected co-precipitation of Bre1, with the D45K charge reversal eliminating Bre1 co-precipitation and causing severe *in vivo* reduction in H2Bub1 and a telomeric silencing defect (Figure 3B–D; Supplementary Figure S15). Further inspection of the crystal structure showed that Rad6 D45 contacts Bre1 R176

(Figure 2A, B), and mutating Bre1 R176 also reduced Rad6 binding (Figure 2D).

Interestingly, co-IP showed that certain mutations at or near the interface—such as alanine substitution at G42 or T46, or the cancer-relevant substitution at P43 or P47—led to increased Rad6–Bre1 interaction (Figure 3A, B, E). Surprisingly, despite their increase in Bre1 binding, all these mutations led to a decrease in H2Bub1 levels and a silencing defect when expressed in yeast (Figure 3C, D, F, G; Supplementary Figure S15). SEC-MALS showed that the rad6-P43L–Bre1^{R6BR} complex had a higher molar mass compared with the Rad6–Bre1 complex (Supplementary Figure S4), suggesting that the rad6-P43L mutation alters the dynamic equilibrium with the Bre1^{R6BR} dimer and stabilizes the protein complex. In an effort to visualize the structural basis for enhanced affinity, we determined the crystal structure of rad6-P43L with Bre1^{R6BR} (Supplementary Table S1). However, this structure was identical to the native complex at the 3.1 Å resolution obtained (Supplementary Figure S16), indicating that enhanced affinity probably results from subtle changes in the spatial arrangement of the interacting residues rather than a gross change in structure.

We then used BLI to determine the binding kinetics between the Bre1^{R6BR} dimer and either wild-type or a selected set of mutant Rad6 proteins. Mild urea treatment was used to disassemble a co-purified complex of Rad6 and biotinylated Bre1^{R6BR} dimer, with the latter then used as the ligand (Supplementary Figure S17a). Recombinant wild-type and mutant Rad6 were also purified to be used as the analyte (Supplementary Figure S17b). Agreeing well with co-IP results (Figure 3E), BLI showed that a subset of Rad6 mutants (P43 or P47) bound Bre1 with relatively high affinity and low off rate *in vitro* (Figure 3H; Supplementary Figure S17c–f). BLI further confirmed that rad6-E49K and rad6-D45K/E49K/D50K had a severely decreased affinity for Bre1^{R6BR} *in vitro* compared with wild-type Rad6 (Figure 3H; Supplementary Figure S17g, h). Together, these data validate the Rad6 backside, especially the conserved loop-3 region, as being a functionally important binding or docking site for Bre1.

Rad6–Bre1^{R6BR} interface controls nucleosome binding *in vitro*

The C-terminal RING domain of Bre1 is known to bind nucleosomes (73). We investigated the possibility that the N-terminal non-RING domain R6BR region of Bre1 could also function in nucleosome binding by performing molecular docking calculation of Rad6–Bre1^{R6BR} with the yeast nucleosome using MOE software. One of the resulting low −ΔG models placed Rad6's active site C88 in close proximity (7.5 Å) to histone H2B K123, the site of ubiquitination on a nucleosome (Figure 4A). This model indicated contacts of the Bre1^{R6BR} with both DNA and histones (Figure 4A, B), thereby suggesting that Bre1^{R6BR} can contribute to nucleosome binding by the Rad6–Bre1 complex. To directly test this possibility, we performed electrophoretic mobility shift assays (EMSAs) by incubating purified Rad6, Bre1^{R6BR} or Rad6–Bre1^{R6BR} with reconstituted yeast mononucleosomes and resolving the complexes using gel electrophoresis. In contrast to Rad6 alone, incuba-
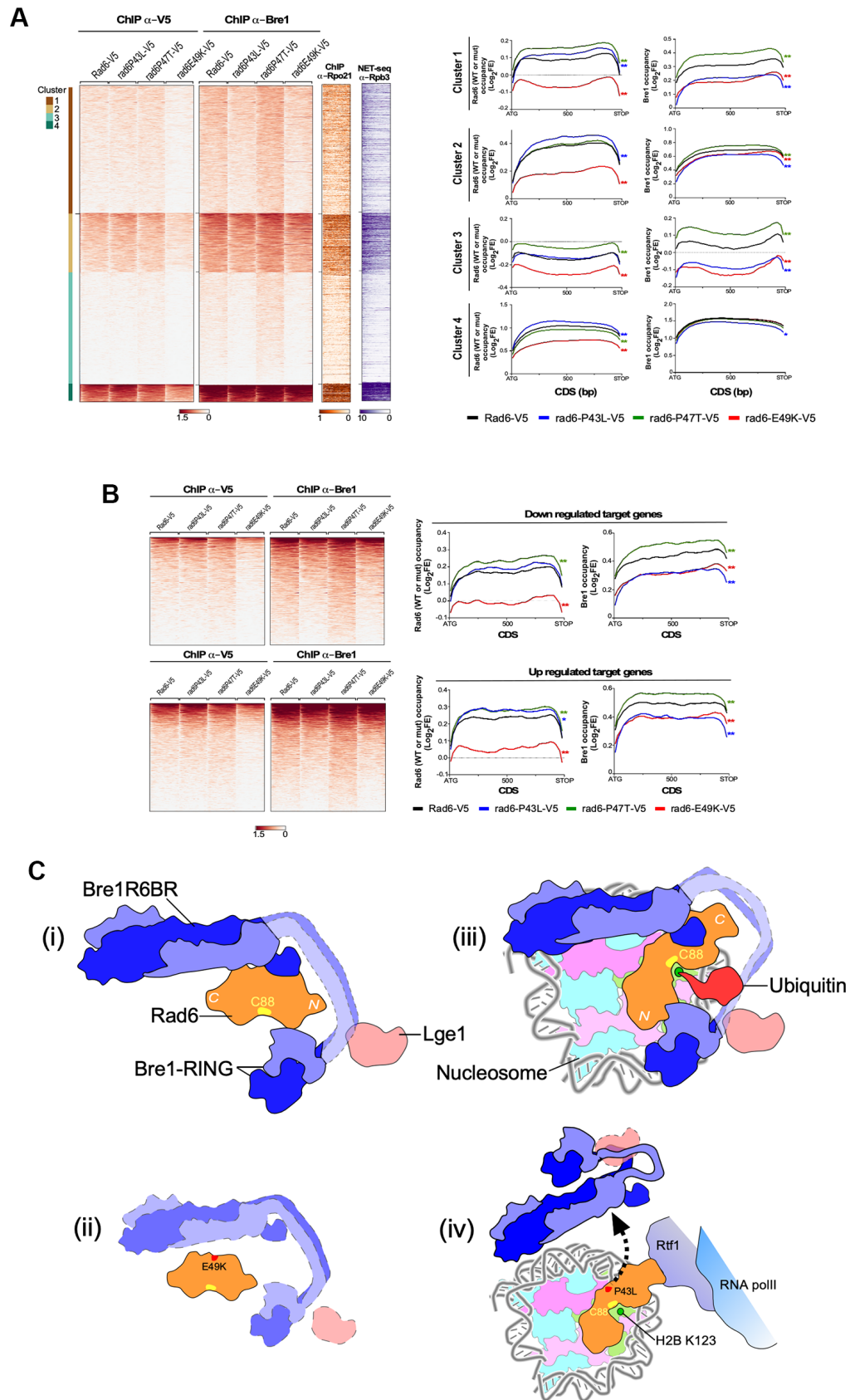
tion of nucleosomes with Bre1^{R6BR} or Rad6–Bre1^{R6BR} led to formation of slow-migrating species along with a concomitant decrease in free nucleosomes, which indicated that the Rad6–Bre1^{R6BR} complex binds nucleosomes. Taken together, this result along with those from the *in vitro* ubiquitination assay (Figure 1D) revealed that association of Rad6 with the Bre1^{R6BR} dimer is sufficient for its substrate nucleosome binding but is insufficient to promote its ubiquitination of nucleosomal H2B.

The *in vivo* H2Bub1 defects of Rad6 P43L and P47T mutants despite their strong Bre1 binding (Figure 3E–H) prompted us to test the ability of the rad6-P43L:Bre1^{R6BR} or rad6-P47T:Bre1^{R6BR} complex to bind nucleosomes *in vitro*. Our mobility shift assays revealed reduction in the binding of rad6-P43L:Bre1^{R6BR} or rad6-P47T:Bre1^{R6BR} mutant complexes to mononucleosomes when compared with the control Rad6:Bre1^{R6BR} complex (Figure 4C). This result reveals a role for the Rad6–Bre1^{R6BR} interaction interface in controlling the nucleosome binding ability of Rad6–Bre1. Moreover, it alludes to differential intermolecular interactions within the Rad6–Bre1 complex in its chromatin-bound and unbound forms.

Rad6–Bre1^{R6BR} interface controls chromatin binding dynamics and transcription *in vivo*

Given their nucleosome binding defects *in vitro*, we then asked whether the loss of H2Bub1 seen with mutation of Rad6 P43 or P47 is due to defects in their binding to Bre1 on chromatin *in vivo*. Hence, we investigated the effect of interface mutations on the chromatin association and transcriptional functions of Rad6 and Bre1. Quantitative ChIP-seq or ChIP-Rx (44) was used to examine the chromatin-bound distribution and occupancies of Bre1 and V5 epitope-tagged wild-type or mutant Rad6, including the cancer-relevant and high-affinity Bre1 binders rad6-P43L and rad6-P47T, and a low-affinity Bre1 binder rad6-E49K (Figures 2 and 3; Supplementary Figure S18). For accurate calibration and quantitative measurement of occupancies using ChIP-Rx, we mixed a defined quantity of a reference genome (74,75), *C. glabrata* expressing Protein AG-tagged cgRad6, with *S. cerevisiae* strains before immunoprecipitation. In this novel approach, the Protein AG-tagged cgRad6-bound genome functions as a 'pan spike-in' compatible with antibodies raised in mouse as well as rabbit (Supplementary Figure S19).

Genome-wide studies have shown that H2Bub1, Rad6 and Bre1 occupy gene bodies in yeast (8,76). We therefore mapped the distribution and occupancies of Bre1 and either wild-type or mutant Rad6 across the coding region of all yeast genes and grouped them using *k*-means clustering (Figure 5A). We also examined the transcriptional status of the genes in these clusters using published datasets for the occupancy of RNA polymerase II (Rpo21) (77), its transcriptional elongation state (Rpb3 NET-seq) (78) and its transcriptional rate (79). Consistent with their well-established connection to gene regulation (76,80), the chromatin occupancies of Rad6 and Bre1 correlate well with the transcription rates of genes in the four clusters (Figure 5A; Supplementary Figure S20). We also performed RNA sequencing (RNA-seq) to measure gene expression in these

Figure 5. Interface residues are important for chromatin binding and transcriptional regulation. (**A**) Left: occupancy changes in V5-tagged wild-type Rad6 or its mutant derivative and Bre1 relative to input across the coding regions of all yeast genes are shown as a log₂ fold enrichment heat map. Genes in rows

strains along with *rad6Δ* or *bre1Δ* null strains for comparison. We defined target genes as transcripts that underwent a ≥1.5-fold change (up or down) in their steady-state levels in the mutants compared with the control (false discovery rate ≤5%) (Supplementary Figure S21; Supplementary Datasheets). We then mapped the distribution and occupancy of Bre1 and Rad6 or its mutants across the coding region of these target genes.

Consistent with impaired Bre1 binding and severely decreased H2Bub1 levels (Supplementary Figures S1b–d and 2a), RNA-seq showed that rad6-E49K had a higher number of up- or down-regulated genes in common with *rad6Δ* and *bre1Δ* than the other mutants (Supplementary Figure S21). Moreover, chromatin occupancies of rad6-E49K and associated Bre1 were significantly decreased across the coding regions of target genes and at genes present in clusters 1, 2 and 3 (Figure 5A, B). These results explain the H2Bub1 defect of the rad6-E49K mutant (Supplementary Figure S1) and further validate the crystal structure interface as being critical for the biological interaction (Figures 1–3).

Matching well with their high-affinity *in vitro* binding (Figure 3H), the chromatin occupancy of rad6-P47T and its associated Bre1 was increased at target genes (Figure 5A, B). Notably, rad6-P47T retained ∼50% of the H2Bub1 level (Figure 3F, G), which contrasts with severely decreased H2Bub1 levels of rad6-P43L that binds Bre1 with similar increased affinity to rad6-P47T and rad6-E49K that displays weaker Bre1 binding (Figure 3). Despite the substantial retention of H2Bub1, a higher number of transcripts were deregulated in rad6-P47T compared with rad6-P43L, and more transcripts were up-regulated in rad6-P47T compared with rad6-E49K (Supplementary Figure S21). Moreover, unlike at target up- or down-regulated genes, the chromatin occupancy of the rad6-P47T–Bre1 complex is similar or decreased when compared with wild-type Rad6 in clusters 2 and 4 that include genes with high transcription rates (Supplementary Figure S20a). While this result agrees well with the reduced *in vitro* nucleosome binding observed for the recombinant rad6-P47T–Bre1^{R6BR} complex (Figure 4C), the increased occupancy for rad6-P47T and Bre1 *in vivo* at clusters 1 and 3 and at target up- or down-regulated genes indicates possible differences in the conformations of the full-length versus truncated Rad6–Bre1 protein complexes and differences in their binding properties to recombinant ver-

sus native nucleosomes. Nevertheless, the high chromatin retention of rad6-P47T–Bre1 causes transcriptional deregulation at target genes (Supplementary Figure S21), which also indicates an impairment of a functionally important conformational transition following chromatin binding or upon chromatin unloading for this cancer-relevant Rad6–Bre1 interface mutation.

The chromatin occupancy of rad6-P43L remained either unchanged or increased at target genes and at all four gene clusters (Figure 5A, B). Remarkably, however, despite the strong rad6-P43L–Bre1 binding seen in co-IP and BLI experiments (Figure 3E, G, H; Supplementary Figure S2), the chromatin occupancy of Bre1 in the rad6-P43L mutant is decreased at target genes and across all four *k*-means clusters (Figure 5A, B). These results suggests that rad6-P43L binds Bre1 tightly in isolation, but binding is disrupted on chromatin, which would explain the low levels of H2Bub1 seen *in vivo* (Figure 3F; Supplementary Figure S1B, C) and the reduced nucleosome binding seen *in vitro* (Figure 4C). Taken together, these intriguing results suggest the possibility of a functionally crucial conformational change for Rad6–Bre1 upon their binding to substrate nucleosome that is incompatible with the cancer-relevant rad6-P43L mutation.

DISCUSSION

The conserved Rad6–Bre1–Lge1 subunits of the yeast HUC complex are responsible for histone H2B monoubiquitination, a master regulatory epigenetic mark with well-established functions in gene transcription and other nuclear processes. A non-RING N-terminal Rad6-binding region (R6BR) within Bre1 and nucleosome binding by Bre1's C-terminal RING domains were previously reported (16–17,73). Barring these studies and despite their functional importance, the molecular details regarding how a single Rad6 E2 enzyme binds a homodimer of the Bre1 E3 ligase, and how this key E2–E3 complex acts on a nucleosomal or chromatin template during transcription, have remained to be elucidated. We now provide insight into the structure and chromatin-based biological functions for the interaction between a homodimer of Bre1's N-terminal coiled-coil domain (or R6BR) and a conserved loop-3 in E2 Rad6's 'backside' region.

---

are organized into four *k*-means cluster. Columns represent 50 bp windows across coding regions (1000 bp) from start (ATG) to stop codons. Heat maps are also shown for RNA polymerase II occupancy at the four *k*-means clusters, using published data for Rpo21 ChIP-seq (78) or Rpb3 NET-seq (79). Right: average mean profiles for wild-type or mutant Rad6 and Bre1 occupancies across the coding regions of genes in the four *k*-means clusters are shown. (**B**) Heat maps (left) and average mean profiles (right) of wild-type or mutant Rad6 and Bre1 occupancies across the coding regions of up- or down-regulated target genes are shown. Statistical significance calculated using ANOVA test, *P-value <0.05; **P-value <10^{-4}. Two independent ChIP-Rx experiments were performed. CDS, coding sequence. (**C**) Proposed models for assembly and substrate recognition for the HUC complex. (i) The N-terminal R6BR regions of Bre1 associate with loop-3 on Rad6's backside region. Bre1 subunits homodimerize via extensive intermolecular interactions. The Bre1 RING domains make contacts with the front face of Rad6 close to its catalytic pocket. Association with Rad6 stabilizes Bre1. Lge1 associates with the Rad6-bound Bre1 to become stabilized and to complete HUC complex formation. Unlike the central region (opaque and dotted line), Bre1's R6BR and RING domains are shown with a solid black line as crystal structures are available. (ii) Interaction-disrupting mutations at the Rad6–Bre1 interface, such as rad6-E49K, inhibit complex assembly, leading to degradation of Bre1 and Lge1. (iii) The HUC complex is recruited onto chromatin during transcription owing to the interaction between Rad6 and the Rtf1 subunit of the RNA polymerase II-associated Paf1 elongation complex. On chromatin, the Bre1^{R6BR} dimer straps the nucleosome to orient Rad6 towards the H2B C-terminus. Interaction of the Bre1-RING domains with the acidic patch on histones H2A–H2B causes a conformational change in Rad6 to bring its active site C88 near the target site K123 on histone H2B. Bre1 and Lge1 then promote the transfer of a single ubiquitin onto histone H2B K123. (iv) The otherwise strong interaction of Bre1 with the cancer-relevant rad6-P43L mutation in solution is incompatible with the conformational change adopted by Rad6 following nucleosome binding, leading to dissociation of Bre1 from the HUC complex. Rad6 remains bound to chromatin owing to its association with the Paf1 complex.

The RING domain of E3 ligases in general contacts the catalytic pocket of their partner E2s to promote ubiquitin transfer (56,81–83). Some RING E3 ligases, such as gp78 and Rad18, contain additional domains that control ubiquitination via binding to their cognate E2's so-called backside region (56,82), which is an interaction interface on E2 enzymes that regulates their catalytic activity via allostery or by outcompeting the weak non-canonical binding of ubiquitin (61,81). Despite the central helix ($\alpha 1'$) of Bre1^{R6BR} showing structural similarity with the backside-binding helices of gp78 and Cue1 that promote ubiquitin chain formation (Supplementary Figure S9), Bre1^{R6BR} in fact restricts Rad6's polyubiquitination activity *in vitro* (17,61) (Figure 1D). One explanation is that, like Rad18–R6BD (71), the strong backside binding of Bre1^{R6BR} (K_d 112 nM) outcompetes the relatively weak non-canonical backside binding of ubiquitin (K_d 1 mM) implicated in polyubiquitination (61). Alternatively, the backside binding of a second helix ($\alpha 4$) unique to Bre1^{R6BR} might act as a dampener of processive ubiquitination. Thus, based our studies and those of others, we surmise that the backside binding of Bre1^{R6BR} could act in part in converting Rad6 from a polyubiquitinase to a H2B monoubiquitinase.

Many E3s interact transiently with their partner E2s (84). In contrast, Bre1^{R6BR} forms a stable association with Rad6. The stability of Bre1 *in vivo* is also dependent on its interaction with Rad6 (72) (Figure 2E, F). Moreover, co-expression of Rad6 stabilizes Bre1^{R6BR} in bacteria (Shukla and Chandrasekharan, unpublished observation). Thus, Rad6 appears to be an obligate partner of Bre1. The stability of Lge1, the third subunit of the HUC complex, was shown to be dependent on Bre1 (85). Thus, a model for stepwise assembly of the HUC complex can be envisaged (Figure 5C): Bre1's R36 and/or R180 make the initial high-affinity charge-based contact with E49 and D50 in the backside loop-3 of Rad6. This is followed by additional stabilizing interactions including those between Bre1's R176 and Rad6's D45 and between Bre1's K31 and Rad6's W149 and D150 (17) (Figure 2A; Supplementary Figure S11c). The HUC complex assembly is then completed upon binding of Lge1 to Bre1. In line with this hierarchical assembly model, mutations in the Rad6–Bre1 interface, such as rad6-E49K, disrupt the HUC complex formation and compromise the stability of Bre1 and Lge1 subunits (Figure 5C). A striking aspect in our Rad6–Bre1^{R6BR} structure is the asymmetry displayed by the Bre1^{R6BR} homodimer, which is in stark contrast to the symmetry shown by Bre1's RING domain homodimer (86). Thus, the heterometric conformation of the Bre1^{R6BR} homodimer represents a remarkable structural adaptation and suggests distinct structural roles for the subunits of the heterodimeric Bre1 homologs in human (RNF20/RNF40) and fission yeast (Brl1/Brl2). Consistent with this model, loss of Brl1 or Brl2 in fission yeast or of RNF20 or RNF40 in mammalian cells adversely affects H2Bub1 levels (18,87–88).

The asymmetric Bre1^{R6BR} dimer binding to a single Rad6 is unique when compared with that reported for other histone-modifying E3s, such as, Ring1A–Bmi1 in the PRC1 complex and BRCA1–BARD1, where the RING heterodimers contain one E2-binding RING (89–91), and RNF168, which is a monomeric RING (92). To date, structural and/or functional studies have shown nucleosome binding for only the E3 RING domain(s) in the different histone-modifying E2–E3 enzymes including PRC1 and HUC complexes (73,89–90). Thus, we report for the first time that a non-RING region of an E3 ligase can also confer nucleosome binding to its partner E2 enzyme (Figure 4B). Despite conferring nucleosome binding ability, the Bre1^{R6BR} dimer is insufficient to support its monoubiquitination of nucleosomal H2B (Figure 1D). Therefore, other regions of Bre1, such as the RING domain, are probably needed for conjugating ubiquitin onto H2B K123. Indeed, a Rad6–Bre1^{RING} chimeric fusion protein binds nucleosomes and supports histone H2B monoubiquitination (73). This study also reported an interaction between Bre1's RING domain and the acidic patch on histones H2A–H2B in a nucleosome and proposed a role for this interaction in target site selection by Rad6 on a nucleosome (73) (Supplementary Figure S22a). Overall, our findings along with this study suggest that both Bre1's N-terminal R6BR and the C-terminal RING domains could contribute to substrate nucleosome binding, but the RING domain promotes catalytic functions of Rad6 by target site selection and/or via other mechanisms.

Structures of nucleosome-bound E2–E3 complexes reported to date all show the E3 RING domain(s) binding to the acidic patch on a nucleosome (89,91–92). Like the Bre1 RING domain (73), the nucleosome acidic patch is also bound by the RING domains of Ring1a/Bmi1 E3 ligases of the PRC1 complex involved in monoubiquitinating histone H2A K119 (89), which, however, is present at the opposite end in a nucleosome relative to histone H2B K120 (human equivalent to yeast H2B K123). These observations therefore allude to hitherto unknown region(s) within Bre1 other than its RING domain that can contribute to target site selection by the HUC complex on a nucleosome. Our molecular docking and *in vitro* nucleosome binding assays now implicate the N-terminal Bre1 R6BR domain as the region that can confer directionality to Rad6 and orient it towards the H2B C-terminus (Figure 4A, B).

Superposition of the Rad6–Bre1^{R6BR} co-crystal structure with the proposed *in silico* model for the nucleosome-bound Rad6–Bre1^{RING} fusion protein suggests that histone H2B monoubiquitination by the HUC complex might involve the binding of Bre1^{R6BR} to an adjacent nucleosome (Supplementary Figure S22b). However, molecular docking of the Rad6–Bre1^{R6BR} complex onto a nucleosome (Figure 4A), its *in vitro* mononucleosome binding ability (Figure 4B) and a conceivable incompatibility of the HUC complex to bind dinucleosomes due to its known interaction with the Paf1 elongation complex (76) and traveling with the transcribing RNA polymerase II (80) altogether provoke the following model for nucleosome binding and histone H2B monoubiquitination by the HUC complex during transcription (Figure 5C). Following recruitment onto chromatin, active Rad6 is oriented away from histone H2A and brought close to the histone H2B C-terminus by the binding and traversing of the Bre1^{R6BR} dimer across a mononucleosome. Binding of the Bre1 RING domain to the acidic patch on histones H2A–H2B then places Rad6's ubiquitin-charged active site C88 near H2B K123 for the nucleophilic attack. Backside binding of Bre1^{R6BR}, and perhaps Lge1,

then restricts Rad6's activity to transfer a single ubiquitin onto H2B K123. Future structural investigations will resolve these proposed models for the substrate nucleosome binding of the HUC complex.

As stated above, the RING domains of E3 ligases contact the front face close to the catalytic pocket of their partner E2 enzymes (56,81–83). However, our nucleosome-docked model for Rad6–Bre1^{R6BR} shows that Rad6's front face is distant from the acid patch-anchored Bre1 RING domains (Supplementary Figure S22c). To reconcile this point, we further propose that the Bre1-bound Rad6 probably undergoes a conformational change on the nucleosome, owing to the binding of the Bre1 RING domain to the acidic groove on histones H2A–H2B (73). The backside loop-3 of Rad6, which is at the crux of the Rad6–Bre1 interaction interface (Figures 1–3), could be envisaged to act as a pivot that allows Rad6 to undergo this conformational change while still retaining Bre1 binding. Certain mutations in loop-3 of Rad6, such as the cancer-relevant P43L and P47T, are likely to be incompatible with this conformational change, leading to the release of Bre1 from Rad6, which however remains associated with chromatin owing to its interaction with the Rtf1 subunit of the Paf1 elongation complex (76) (Figure 5C). Importantly, our studies show that certain cancer-relevant and interaction-interface mutations in Rad6 increase Rad6–Bre1 association in solution but disrupt it on chromatin, thus revealing for the first time a novel mode of pleiotropy for disease-relevant mutations that differentially influence a protein's functions in its chromatin-bound and unbound states. In summary, we provide for the first time both structural details and functional nuances for the key Rad6–Bre1 E2–E3 enzymes involved in histone H2B ubiquitination.

DATA AVAILABILITY

Rpo21 ChIP-seq (77) and NET-seq (78) data were retrieved from ArrayExpress (E-MEXP-1677) and GEO (GSM617027) databases, respectively. Transcription rates for yeast genes were obtained from http://www.wi.mit.edu/young/expression.html (79). The mutation resource for the P43L and P43T mutations in UBE2A and P47T mutation in UBE2B can be accessed through the COSMIC database (http://cancer.sanger.uk) under the genomic mutation IDs of COSV60636837, COSV60636753 and COSV54760895, respectively. Atomic coordinates and structure factors for the reported crystal structures of Rad6–Bre1^{R6BR} and rad6-P43L–Bre1^{R6BR} complexes have been deposited in the RCSB Protein Data Bank (RCSB PDB) under accession codes 7UV8 and 7UVC, respectively. ChIP-seq and RNA-seq data generated have been deposited at the NCBI Gene Expression Omnibus (GEO) under accession number GSE139634.

SUPPLEMENTARY DATA

Supplementary Data are available at NAR Online.

ACKNOWLEDGEMENTS

FUNDING

REFERENCES

1. Mirabella,A.C., Foster,B.M. and Bartke,T. (2016) Chromatin deregulation in disease. *Chromosoma*, **125**, 75–93.
2. Audia,J.E. and Campbell,R.M. (2016) Histone modifications and cancer. *Cold Spring Harb. Perspect. Biol.*, **8**, a019521.
3. Bonnet,J., Devys,D. and Tora,L. (2014) Histone H2B ubiquitination: signaling not scrapping. *Drug Discov. Today Technol.*, **12**, e19–e27.
4. Fuchs,G. and Oren,M. (2014) Writing and reading H2B monoubiquitylation. *Biochim. Biophys. Acta*, **1839**, 694–701.
5. Hung,S.H., Wong,R.P., Ulrich,H.D. and Kao,C.F. (2017) Monoubiquitylation of histone H2B contributes to the bypass of DNA damage during and after DNA replication. *Proc. Natl Acad. Sci. USA*, **114**, E2205–E2214.
6. Chandrasekharan,M.B., Huang,F. and Sun,Z.W. (2009) Ubiquitination of histone H2B regulates chromatin dynamics by enhancing nucleosome stability. *Proc. Natl Acad. Sci. USA*, **106**, 16686–16691.
7. Fleming,A.B., Kao,C.F., Hillyer,C., Pikaart,M. and Osley,M.A. (2008) H2B ubiquitylation plays a role in nucleosome dynamics during transcription elongation. *Mol. Cell*, **31**, 57–66.
8. Batta,K., Zhang,Z., Yen,K., Goffman,D.B. and Pugh,B.F. (2011) Genome-wide function of H2B ubiquitylation in promoter and genic regions. *Genes Dev.*, **25**, 2254–2265.
9. Nakanishi,S., Lee,J.S., Gardner,K.E., Gardner,J.M., Takahashi,Y.H., Chandrasekharan,M.B., Sun,Z.W., Osley,M.A., Strahl,B.D., Jaspersen,S.L. *et al.* (2009) Histone H2BK123 monoubiquitination is the critical determinant for H3K4 and H3K79 trimethylation by COMPASS and Dot1. *J. Cell Biol.*, **186**, 371–377.
10. Dover,J., Schneider,J., Tawiah-Boateng,M.A., Wood,A., Dean,K., Johnston,M. and Shilatifard,A. (2002) Methylation of histone H3 by COMPASS requires ubiquitination of histone H2B by Rad6. *J. Biol. Chem.*, **277**, 28368–28371.

11. Sun,Z.W. and Allis,C.D. (2002) Ubiquitination of histone H2B regulates H3 methylation and gene silencing in yeast. *Nature*, **418**, 104–108.

12. Briggs,S.D., Xiao,T., Sun,Z.W., Caldwell,J.A., Shabanowitz,J., Hunt,D.F., Allis,C.D. and Strahl,B.D. (2002) Gene silencing: trans-histone regulatory pathway in chromatin. *Nature*, **418**, 498.

13. Hwang,W.W., Venkatasubrahmanyam,S., Ianculescu,A.G., Tong,A., Boone,C. and Madhani,H.D. (2003) A conserved RING finger protein required for histone H2B monoubiquitination and cell size control. *Mol. Cell*, **11**, 261–266.

14. Wood,A., Krogan,N.J., Dover,J., Schneider,J., Heidt,J., Boateng,M.A., Dean,K., Golshani,A., Zhang,Y., Greenblatt,J.F. *et al.* (2003) Bre1, an E3 ubiquitin ligase required for recruitment and substrate selection of Rad6 at a promoter. *Mol. Cell*, **11**, 267–274.

15. Zhang,F. and Yu,X. (2011) WAC, a functional partner of RNF20/40, regulates histone H2B ubiquitination and gene transcription. *Mol. Cell*, **41**, 384–397.

16. Kim,J. and Roeder,R.G. (2009) Direct Bre1–Paf1 complex interactions and RING finger-independent Bre1–Rad6 interactions mediate histone H2B ubiquitylation in yeast. *J. Biol. Chem.*, **284**, 20582–20592.

17. Turco,E., Gallego,L.D., Schneider,M. and Kohler,A. (2015) Monoubiquitination of histone H2B is intrinsic to the Bre1 RING domain–Rad6 interaction and augmented by a second Rad6-binding site on Bre1. *J. Biol. Chem.*, **290**, 5298–5310.

18. Zofall,M. and Grewal,S.I. (2007) HULC, a histone H2B ubiquitinating complex, modulates heterochromatin independent of histone methylation in fission yeast. *J. Biol. Chem.*, **282**, 14065–14072.

19. Li,M.Z. and Elledge,S.J. (2012) SLIC: a method for sequence- and ligation-independent cloning. *Methods Mol. Biol.*, **852**, 51–59.

20. Mumberg,D., Muller,R. and Funk,M. (1995) Yeast vectors for the controlled expression of heterologous proteins in different genetic backgrounds. *Gene*, **156**, 119–122.

21. Fairhead,M. and Howarth,M. (2015) Site-specific biotinylation of purified proteins using BirA. *Methods Mol. Biol.*, **1266**, 171–184.

22. Zordan,R.E., Ren,Y., Pan,S.J., Rotondo,G., De Las Penas,A., Iluore,J. and Cormack,B.P. (2013) Expression plasmids for use in *Candida glabrata*. *G3 (Bethesda)*, **3**, 1675–1686.

23. Goldstein,A.L. and McCusker,J.H. (1999) Three new dominant drug resistance cassettes for gene disruption in *Saccharomyces cerevisiae*. *Yeast*, **15**, 1541–1553.

24. Sikorski,R.S. and Hieter,P. (1989) A system of shuttle vectors and yeast host strains designed for efficient manipulation of DNA in *Saccharomyces cerevisiae*. *Genetics*, **122**, 19–27.

25. Sharma,S., T.,S. and Bhatia,K. (1999) Preparation and characterization of the N and C monoferric lobes of buffalo lactoferrin produced by proteolysis using proteinase K. *J. Dairy Res.*, **66**, 81–90.

26. Evans,P.R. and Murshudov,G.N. (2013) How good are my data and what is the resolution?*Acta Crystallogr. D Biol. Crystallogr.*, **69**, 1204–1214.

27. Pannu,N.S., Waterreus,W.J., Skubak,P., Sikharulidze,I., Abrahams,J.P. and de Graaff,R.A. (2011) Recent advances in the CRANK software suite for experimental phasing. *Acta Crystallogr. D Biol. Crystallogr.*, **67**, 331–337.

28. Cowtan,K. (2006) The Buccaneer software for automated model building. 1. Tracing protein chains. *Acta Crystallogr. D Biol. Crystallogr.*, **62**, 1002–1011.

29. Wang,J., Li,Y. and Modis,Y. (2014) Exploiting subtle structural differences in heavy-atom derivatives for experimental phasing. *Acta Crystallogr. D Biol. Crystallogr.*, **70**, 1873–1883.

30. Terwilliger,T.C., Grosse-Kunstleve,R.W., Afonine,P.V., Moriarty,N.W., Zwart,P.H., Hung,L.W., Read,R.J. and Adams,P.D. (2008) Iterative model building, structure refinement and density modification with the PHENIX AutoBuild wizard. *Acta Crystallogr. D Biol. Crystallogr.*, **64**, 61–69.

31. Emsley,P. and Cowtan,K. (2004) Coot: model-building tools for molecular graphics. *Acta Crystallogr. D Biol. Crystallogr.*, **60**, 2126–2132.

32. Adams,P.D., Grosse-Kunstleve,R.W., Hung,L.W., Ioerger,T.R., McCoy,A.J., Moriarty,N.W., Read,R.J., Sacchettini,J.C., Sauter,N.K. and Terwilliger,T.C. (2002) PHENIX: building new software for automated crystallographic structure determination. *Acta Crystallogr. D Biol. Crystallogr.*, **58**, 1948–1954.

33. McCoy,A.J., Grosse-Kunstleve,R.W., Adams,P.D., Winn,M.D., Storoni,L.C. and Read,R.J. (2007) Phaser crystallographic software. *J. Appl. Crystallogr*, **40**, 658–674.

34. Laskowski,R.A., MacArthur,M.W., Moss,D.S. and Thornton,J.M. (1993) PROCHECK: a program to check the stereochemical quality of protein structures. *J. Appl. Crystallogr.,***26**, 283–291.

35. Krissinel,E. and Henrick,K. (2004) Secondary-structure matching (SSM), a new tool for fast protein structure alignment in three dimensions. *Acta Crystallogr. D Biol. Crystallogr.*, **60**, 2256–2268.

36. Hubbard,S. and Thornton,J. (1993) '*NACCESS*', computer program. Department of Biochemistry and Molecular Biology, University College, London.

37. Vangone,A., Spinelli,R., Scarano,V., Cavallo,L. and Oliva,R. (2011) COCOMAPS: a web application to analyze and visualize contacts at the interface of biomolecular complexes. *Bioinformatics*, **27**, 2915–2916.

38. Laskowski,R.A. and Swindells,M.B. (2011) LigPlot+: multiple ligand–protein interaction diagrams for drug discovery. *J. Chem. Inf. Model*, **51**, 2778–2786.

39. Chandrasekharan,M.B., Huang,F. and Sun,Z.W. (2011) Decoding the trans-histone crosstalk: methods to analyze H2B ubiquitination, H3 methylation and their regulatory factors. *Methods*, **54**, 304–314.

40. Leng,A.M., Radmall,K.S., Shukla,P.K. and Chandrasekharan,M.B. (2022) Quantitative assessment of histone H2B monoubiquitination in yeast using immunoblotting. *Methods Protoc.*, **5**, 74.

41. Wittmeyer,J., Saha,A. and Cairns,B. (2004) DNA translocation and nucleosome remodeling assays by the RSC chromatin remodeling complex. *Methods Enzymol.*, **377**, 322–343.

42. Dyer,P.N., Edayathumangalam,R.S., White,C.L., Bao,Y., Chakravarthy,S., Muthurajan,U.M. and Luger,K. (2004) Reconstitution of nucleosome core particles from recombinant histones and DNA. *Methods Enzymol.*, **375**, 23–44.

43. Shukla,P.K., Sinha,D., Leng,A.M., Bissell,J.E., Thatipamula,S., Ganguly,R., Radmall,K.S., Skalicky,J.J., Shrieve,D.C. and Chandrasekharan,M.B. (2022) Mutations of Rad6 E2 ubiquitin-conjugating enzymes at alanine-126 in helix-3 affect ubiquitination activity and decrease enzyme stability. *J. Biol. Chem.*, **298**, 102524.

44. Orlando,D.A., Chen,M.W., Brown,V.E., Solanki,S., Choi,Y.J., Olson,E.R., Fritz,C.C., Bradner,J.E. and Guenther,M.G. (2014) Quantitative ChIP-seq normalization reveals global modulation of the epigenome. *Cell Rep.*, **9**, 1163–1170.

45. Yershova,A., Jain,S., Lavalle,S.M. and Mitchell,J.C. (2010) Generating uniform incremental grids on SO(3) using the hopf fibration. *Int. J. Rob. Res.*, **29**, 801–812.

46. Bailly,V., Lamb,J., Sung,P., Prakash,S. and Prakash,L. (1994) Specific complex formation between yeast RAD6 and RAD18 proteins: a potential mechanism for targeting RAD6 ubiquitin-conjugating activity to DNA damage sites. *Genes Dev.*, **8**, 811–820.

47. Andreson,B.L., Gupta,A., Georgieva,B.P. and Rothstein,R. (2010) The ribonucleotide reductase inhibitor, Sml1, is sequentially phosphorylated, ubiquitylated and degraded in response to DNA damage. *Nucleic Acids Res.*, **38**, 6490–6501.

48. Xie,Y. and Varshavsky,A. (1999) The E2–E3 interaction in the N-end rule pathway: the RING-H2 finger of E3 is required for the synthesis of multiubiquitin chain. *EMBO J.*, **18**, 6832–6844.

49. Freiberg,G., Mesecar,A.D., Huang,H., Hong,J.Y. and Liebman,S.W. (2000) Characterization of novel rad6/ubc2 ubiquitin-conjugating enzyme mutants in yeast. *Curr. Genet.*, **37**, 221–233.

50. Krogan,N.J., Dover,J., Khorrami,S., Greenblatt,J.F., Schneider,J., Johnston,M. and Shilatifard,A. (2002) COMPASS, a histone H3 (Lysine 4) methyltransferase required for telomeric silencing of gene expression. *J. Biol. Chem.*, **277**, 10753–10755.

51. Chandrasekharan,M.B., Huang,F., Chen,Y.C. and Sun,Z.W. (2010) Histone H2B C-terminal helix mediates trans-histone H3K4 methylation independent of H2B ubiquitination. *Mol. Cell Biol.*, **30**, 3216–3232.

52. Bamford,S., Dawson,E., Forbes,S., Clements,J., Pettett,R., Dogan,A., Flanagan,A., Teague,J., Futreal,P.A., Stratton,M.R. *et al.* (2004) The COSMIC (Catalogue of Somatic Mutations in Cancer) database and website. *Br. J. Cancer*, **91**, 355–358.

53. Kim,J., Guermah,M., McGinty,R.K., Lee,J.S., Tang,Z., Milne,T.A., Shilatifard,A., Muir,T.W. and Roeder,R.G. (2009) RAD6-mediated

transcription-coupled H2B ubiquitylation directly stimulates H3K4 methylation in human cells. *Cell*, **137**, 459–471.

54. Brzovic,P.S., Lissounov,A., Christensen,D.E., Hoyt,D.W. and Klevit,R.E. (2006) A UbcH5/ubiquitin noncovalent complex is required for processive BRCA1-directed ubiquitination. *Mol. Cell*, **21**, 873–880.

55. Stewart,M.D., Ritterhoff,T., Klevit,R.E. and Brzovic,P.S. (2016) E2 enzymes: more than just middle men. *Cell Res.*, **26**, 423–440.

56. Berndsen,C.E. and Wolberger,C. (2014) New insights into ubiquitin E3 ligase mechanism. *Nat. Struct. Mol. Biol.*, **21**, 301–307.

57. Pan,M., Zheng,Q., Wang,T., Liang,L., Mao,J., Zuo,C., Ding,R., Ai,H., Xie,Y., Si,D. *et al.* (2021) Structural insights into Ubr1-mediated N-degron polyubiquitination. *Nature*, **600**, 334–338.

58. Buetow,L. and Huang,D.T. (2016) Structural insights into the catalysis and regulation of E3 ubiquitin ligases. *Nat. Rev. Mol. Cell Biol.*, **17**, 626–642.

59. Das,R., Mariano,J., Tsai,Y.C., Kalathur,R.C., Kostova,Z., Li,J., Tarasov,S.G., McFeeters,R.L., Altieri,A.S., Ji,X. *et al.* (2009) Allosteric activation of E2-RING finger-mediated ubiquitylation by a structurally defined specific E2-binding region of gp78. *Mol. Cell*, **34**, 674–685.

60. Worthylake,D.K., Prakash,S., Prakash,L. and Hill,C.P. (1998) Crystal structure of the Saccharomyces cerevisiae ubiquitin-conjugating enzyme Rad6 at 2.6 Å resolution. *J. Biol. Chem.*, **273**, 6271–6276.

61. Kumar,P., Magala,P., Geiger-Schuller,K.R., Majumdar,A., Tolman,J.R. and Wolberger,C. (2015) Role of a non-canonical surface of Rad6 in ubiquitin conjugating activity. *Nucleic Acids Res.*, **43**, 9039–9050.

62. de Oliveira,J.F., do Prado,P.F.V., da Costa,S.S., Sforca,M.L., Canateli,C., Ranzani,A.T., Maschietto,M., de Oliveira,P.S.L., Otto,P.A., Klevit,R.E. *et al.* (2019) Mechanistic insights revealed by a UBE2A mutation linked to intellectual disability. *Nat. Chem. Biol.*, **15**, 62–70.

63. Ju,T., Bocik,W., Majumdar,A. and Tolman,J.R. (2010) Solution structure and dynamics of human ubiquitin conjugating enzyme Ube2g2. *Proteins*, **78**, 1291–1301.

64. Sarcevic,B., Mawson,A., Baker,R.T. and Sutherland,R.L. (2002) Regulation of the ubiquitin-conjugating enzyme hHR6A by CDK-mediated phosphorylation. *EMBO J.*, **21**, 2009–2018.

65. Shchebet,A., Karpiuk,O., Kremmer,E., Eick,D. and Johnsen,S.A. (2012) Phosphorylation by cyclin-dependent kinase-9 controls ubiquitin-conjugating enzyme-2A function. *Cell Cycle*, **11**, 2122–2127.

66. Wood,A., Schneider,J., Dover,J., Johnston,M. and Shilatifard,A. (2005) The Bur1/Bur2 complex is required for histone H2B monoubiquitination by Rad6/Bre1 and histone methylation by COMPASS. *Mol. Cell*, **20**, 589–599.

67. Sung,P., Prakash,S. and Prakash,L. (1988) The RAD6 protein of *Saccharomyces cerevisiae* polyubiquitinates histones, and its acidic domain mediates this activity. *Genes Dev.*, **2**, 1476–1485.

68. Jentsch,S., McGrath,J.P. and Varshavsky,A. (1987) The yeast DNA repair gene RAD6 encodes a ubiquitin-conjugating enzyme. *Nature*, **329**, 131–134.

69. Metzger,M.B., Liang,Y.H., Das,R., Mariano,J., Li,S., Li,J., Kostova,Z., Byrd,R.A., Ji,X. and Weissman,A.M. (2013) A structurally unique E2-binding domain activates ubiquitination by the ERAD E2, Ubc7p, through multiple mechanisms. *Mol. Cell*, **50**, 516–527.

70. Li,S., Liang,Y.H., Mariano,J., Metzger,M.B., Stringer,D.K., Hristova,V.A., Li,J., Randazzo,P.A., Tsai,Y.C., Ji,X. *et al.* (2015) Insights into ubiquitination from the unique clamp-like binding of the RING E3 AO7 to the E2 UbcH5B. *J. Biol. Chem.*, **290**, 30225–30239.

71. Hibbert,R.G., Huang,A., Boelens,R. and Sixma,T.K. (2011) E3 ligase Rad18 promotes monoubiquitination rather than ubiquitin chain formation by E2 enzyme Rad6. *Proc. Natl Acad. Sci. USA*, **108**, 5590–5595.

72. Wozniak,G.G. and Strahl,B.D. (2014) Catalysis-dependent stabilization of Bre1 fine-tunes histone H2B ubiquitylation to regulate gene transcription. *Genes Dev.*, **28**, 1647–1652.

73. Gallego,L.D., Ghodgaonkar Steger,M., Polyansky,A.A., Schubert,T., Zagrovic,B., Zheng,N., Clausen,T., Herzog,F. and Kohler,A. (2016) Structural mechanism for the recognition and ubiquitination of a single nucleosome residue by Rad6–Bre1. *Proc. Natl Acad. Sci. USA*, **113**, 10553–10558.

74. Hu,B., Petela,N., Kurze,A., Chan,K.L., Chapard,C. and Nasmyth,K. (2015) Biological chromodynamics: a general method for measuring protein occupancy across the genome by calibrating ChIP-seq. *Nucleic Acids Res.*, **43**, e132.

75. Ramakrishnan,S., Pokhrel,S., Palani,S., Pflueger,C., Parnell,T.J., Cairns,B.R., Bhaskara,S. and Chandrasekharan,M.B. (2016) Counteracting H3K4 methylation modulators Set1 and Jhd2 co-regulate chromatin dynamics and gene transcription. *Nat. Commun.*, **7**, 11949.

76. Van Oss,S.B., Shirra,M.K., Bataille,A.R., Wier,A.D., Yen,K., Vinayachandran,V., Byeon,I.L., Cucinotta,C.E., Heroux,A., Jeon,J. *et al.* (2016) The histone modification domain of Paf1 complex subunit Rtf1 directly stimulates H2B ubiquitylation through an interaction with Rad6. *Mol. Cell*, **64**, 815–825.

77. Venters,B.J. and Pugh,B.F. (2009) A canonical promoter organization of the transcription machinery and its regulators in the Saccharomyces genome. *Genome Res.*, **19**, 360–371.

78. Churchman,L.S. and Weissman,J.S. (2011) Nascent transcript sequencing visualizes transcription at nucleotide resolution. *Nature*, **469**, 368–373.

79. Holstege,F.C., Jennings,E.G., Wyrick,J.J., Lee,T.I., Hengartner,C.J., Green,M.R., Golub,T.R., Lander,E.S. and Young,R.A. (1998) Dissecting the regulatory circuitry of a eukaryotic genome. *Cell*, **95**, 717–728.

80. Xiao,T., Kao,C.F., Krogan,N.J., Sun,Z.W., Greenblatt,J.F., Osley,M.A. and Strahl,B.D. (2005) Histone H2B ubiquitylation is associated with elongating RNA polymerase II. *Mol. Cell Biol.*, **25**, 637–651.

81. Metzger,M.B., Pruneda,J.N., Klevit,R.E. and Weissman,A.M. (2014) RING-type E3 ligases: master manipulators of E2 ubiquitin-conjugating enzymes and ubiquitination. *Biochim. Biophys. Acta*, **1843**, 47–60.

82. Gundogdu,M. and Walden,H. (2019) Structural basis of generic versus specific E2–RING E3 interactions in protein ubiquitination. *Protein Sci.*, **28**, 1758–1770.

83. Zheng,N. and Shabek,N. (2017) Ubiquitin ligases: structure, function, and regulation. *Annu. Rev. Biochem.*, **86**, 129–157.

84. Cappadocia,L. and Lima,C.D. (2018) Ubiquitin-like protein conjugation: structures, chemistry, and mechanism. *Chem. Rev.*, **118**, 889–918.

85. Kim,J., An,Y.K., Park,S. and Lee,J.S. (2018) Bre1 mediates the ubiquitination of histone H2B by regulating Lge1 stability. *FEBS Lett.*, **592**, 1565–1574.

86. Kumar,P. and Wolberger,C. (2015) Structure of the yeast Bre1 RING domain. *Proteins*, **83**, 1185–1190.

87. Tanny,J.C., Erdjument-Bromage,H., Tempst,P. and Allis,C.D. (2007) Ubiquitylation of histone H2B controls RNA polymerase II transcription elongation independently of histone H3 methylation. *Genes Dev.*, **21**, 835–847.

88. Kim,J., Hake,S.B. and Roeder,R.G. (2005) The human homolog of yeast BRE1 functions as a transcriptional coactivator through direct activator interactions. *Mol. Cell*, **20**, 759–770.

89. McGinty,R.K., Henrici,R.C. and Tan,S. (2014) Crystal structure of the PRC1 ubiquitylation module bound to the nucleosome. *Nature*, **514**, 591–596.

90. Witus,S.R., Burrell,A.L., Farrell,D.P., Kang,J., Wang,M., Hansen,J.M., Pravat,A., Tuttle,L.M., Stewart,M.D., Brzovic,P.S. *et al.* (2021) BRCA1/BARD1 site-specific ubiquitylation of nucleosomal H2A is directed by BARD1. *Nat. Struct. Mol. Biol.*, **28**, 268–277.

91. Dai,L., Dai,Y., Han,J., Huang,Y., Wang,L., Huang,J. and Zhou,Z. (2021) Structural insight into BRCA1–BARD1 complex recruitment to damaged chromatin. *Mol. Cell*, **81**, 2765–2777.

92. Mattiroli,F., Uckelmann,M., Sahtoe,D.D., van Dijk,W.J. and Sixma,T.K. (2014) The nucleosome acidic patch plays a critical role in RNF168-dependent ubiquitination of histone H2A. *Nat. Commun.*, **5**, 3291.